Separating the Influences of Low-Latitude Warming and Sea Ice Loss on Northern Hemisphere Climate Change

Stephanie Hay, Paul J Kushner, Russell Blackport, Kelly E Mccusker, Thomas Oudar, Lantao Sun, Mark England, Clara Deser, James A Screen, Lorenzo M Polvani, et al.

Separating the Influences of Low-Latitude Warming and Sea Ice Loss on Northern Hemisphere Climate Change

STEPHANIE HAY,[a] PAUL J. KUSHNER,[b] RUSSELL BLACKPORT,[c] KELLY E. MCCUSKER,[d] THOMAS OUDAR,[e] LANTAO SUN,[f] MARK ENGLAND,[g] CLARA DESER,[h] JAMES A. SCREEN,[a] AND LORENZO M. POLVANI[i]

[a] *University of Exeter, Exeter, United Kingdom*
[b] *University of Toronto, Toronto, Ontario, Canada*
[c] *Environment and Climate Change Canada, Victoria, British Columbia, Canada*
[d] *Rhodium Group, New York, New York*
[e] *CNRM, Université de Toulouse, Météo-France, CNRS, Toulouse, France*
[f] *Colorado State University, Fort Collins, Colorado*
[g] *University of Santa Cruz, Santa Cruz, California*
[h] *National Center for Atmospheric Research, Boulder, Colorado*
[i] *Columbia University, New York, New York*

(Manuscript received 5 March 2021, in final form 21 December 2021)

ABSTRACT: Analyzing a multimodel ensemble of coupled climate model simulations forced with Arctic sea ice loss using a two-parameter pattern-scaling technique to remove the cross-coupling between low- and high-latitude responses, the sensitivity to high-latitude sea ice loss is isolated and contrasted to the sensitivity to low-latitude warming. Despite some differences in experimental design, the Northern Hemisphere near-surface atmospheric sensitivity to sea ice loss is found to be robust across models in the cold season; however, a larger intermodel spread is found at the surface in boreal summer, and in the free tropospheric circulation. In contrast, the sensitivity to low-latitude warming is most robust in the free troposphere and in the warm season, with more intermodel spread in the surface ocean and surface heat flux over the Northern Hemisphere. The robust signals associated with sea ice loss include upward turbulent and longwave heat fluxes where sea ice is lost, warming and freshening of the Arctic Ocean, warming of the eastern North Pacific Ocean relative to the western North Pacific with upward turbulent heat fluxes in the Kuroshio Extension, and salinification of the shallow shelf seas of the Arctic Ocean alongside freshening in the subpolar North Atlantic Ocean. In contrast, the robust signals associated with low-latitude warming include intensified ocean warming and upward latent heat fluxes near the western boundary currents, freshening of the Pacific Ocean, salinification of the North Atlantic, and downward sensible and longwave fluxes over the ocean.

KEYWORDS: Atmosphere; Ocean; Arctic; Extratropics; Climate models

1. Introduction

Arctic sea ice loss observed by satellites over the last 40 years is one of the most obvious manifestations of greenhouse warming, and many record low extents have occurred in recent years. The question as to how a shrinking ice cover and corresponding increase in open ocean affects the atmosphere, and the midlatitude climate in particular, remains a topic of debate (e.g., Cohen et al. 2014; Vihma 2014; Barnes and Screen 2015; Overland et al. 2015; Cohen et al. 2020; Blackport et al. 2019; Blackport and Screen 2020). It is difficult to disentangle the forced response to sea ice loss from other concurrent forcings, from general greenhouse warming, and from natural variability. Because there is only a relatively short observational period, and the response to sea ice loss has a low signal-to-noise ratio (Screen et al. 2014; Ogawa et al. 2018; Liang et al. 2020), a popular method, and the one we focus on here, for linking Arctic sea ice loss and climate responses is through dedicated modeling experiments with sufficient sampling to separate the signal from climate noise.

Earlier efforts to isolate the forced response to sea ice loss used atmospheric general circulation models (AGCM) forced with either high or low sea ice cover and diagnosed the response as the difference between the resulting atmospheric patterns (Deser et al. 2010; Screen et al. 2012; Peings and Magnusdottir 2014; Sun et al. 2015). A robust warming of the lower troposphere as in Arctic amplification is found, but there tends to be a model dependence (Screen et al. 2012), and robust signals generally do not extend far beyond the high latitudes. Recently, studies have examined this problem using observed sea ice loss and a multimodel AGCM approach (Ogawa et al. 2018; Liang et al. 2020), and largely confirmed the relatively weak role that Arctic sea ice loss plays in the midlatitudes. However, there is also some evidence that sea ice driven variability is too weak in models (Mori et al. 2019a), a matter that remains up for debate (Mori et al. 2019b; Screen and Blackport 2019b; Zappa et al. 2021).

Several studies have sought to study the forced coupled climate response to sea ice loss for individual models (Deser et al. 2015, 2016; Petrie et al. 2015; Blackport and Kushner 2016, 2017; Smith et al. 2017; England et al. 2020a,b) and others have compared that response with the forced response

Corresponding author: Stephanie Hay, shay@physics.utoronto.ca

DOI: 10.1175/JCLI-D-21-0180.1

to an increase in greenhouse gases under constant sea ice area (Oudar et al. 2017; McCusker et al. 2017; Sun et al. 2018). The inclusion of a fully dynamical ocean is shown to be crucial to obtaining the pattern of "mini-global warming" response to sea ice loss (Deser et al. 2015; Tomas et al. 2016), whereby the zonal-mean temperature response to sea ice loss resembles the response to greenhouse warming with amplified warming over both poles and in the tropical upper troposphere. Screen et al. (2018) showed that there were common features among these different coupled climate model simulations when scaling the atmospheric response per unit sea ice loss and an indirect method of obtaining the response to sea ice loss in CMIP5 simulations confirmed a generally robust response to sea ice loss in wintertime across a larger pool of models (Screen and Blackport 2019a). However, the warming of lower latitudes found in coupled simulations of sea ice loss will induce its own response locally and remotely, which makes interpretation of the source of the midlatitude response in these simulations difficult.

One way we can address this potential issue is to take advantage of the similarity in zonal-mean temperature responses to sea ice loss and greenhouse warming, the aforementioned "mini-global warming" pattern, which motivates the use of two-parameter pattern scaling Blackport and Kushner (2017) to further decompose the coupled response to sea ice loss to obtain pattern-scaled sensitivities to sea ice loss (SIL) and to low-latitude warming (LLW). Hay et al. (2018) was the first multimodel comparison to apply this concept as a tool to improve comparison of uncoordinated experiments of the forced model response to sea ice loss by combining greenhouse gas forcing simulations with sea ice loss simulations and then comparing and contrasting their resulting sensitivities. Hay et al. (2018) focused on the near-surface atmospheric response in two models and found that the sensitivity to SIL was more robust than the sensitivity to LLW in wintertime.

While the use of coupled models has indicated that the ocean's circulation is crucial to reduce the uncertainty in the atmospheric response to Arctic sea ice loss, comparatively little research has focused on the ocean's response itself (e.g., Tomas et al. 2016; Sévellec et al. 2017; Wang et al. 2018; Liu and Fedorov 2019; Liu et al. 2019). The Atlantic meridional overturning circulation (AMOC) is found to weaken (Sévellec et al. 2017; Liu and Fedorov 2019; Liu et al. 2019), and associated northward heat transport is reduced (Tomas et al. 2016; England et al. 2020b).

We make use of the pattern-scaling method and preexisting simulations to examine the intermodel and intermethod differences in the Northern Hemispheric atmospheric and oceanic sensitivities to Arctic SIL and to LLW in five different coupled climate models: CESM1 (Blackport and Kushner 2017), WACCM4 (England et al. 2020b), CanESM2 (McCusker et al. 2017), CNRM-CM5 (Oudar et al. 2017), and GFDL CM3 (Sun et al. 2018). This paper presents a generalization of the two-model analysis of Hay et al. (2018) and both presents the most comprehensive assessment of the atmospheric sensitivity to SIL within the coupled climate response and, for the first time, also includes a multimodel intercomparison of the sensitivities of the surface ocean to Arctic SIL.

This paper is organized as follows: in section 2, we present an overview of the experiments and review the two-parameter pattern scaling technique of Blackport and Kushner (2017), which yields the pattern-scaled sensitivities that we use to characterize the models. In section 3, the atmospheric and oceanic sensitivities are presented. A robust sensitivity to SIL is found in the atmosphere, while a robust sensitivity to LLW is found in the ocean. Section 4 features a more in-depth discussion of some aspects of the results, including the role of SIL in Eurasian cooling and how SIL and LLW can induce negative feedbacks on one another, each within the context of the existing literature. The results are summarized in section 5.

2. Data and methods

Because of the uncoordinated nature of these experiments, a given forced response in this ensemble of opportunity will depend not only on the model but also on the experimental protocol used. We seek to characterize the robustness of the forced responses across so-called *model-experiments (MEs)*, defined as the combination of a particular model and a particular experimental protocol used to drive it (e.g., a radiative perturbation or a sea ice perturbation; a transient versus equilibrated/time slice simulation). A *forced response* is the difference between a control ME and a perturbation ME. Ambiguity is introduced in the midlatitude forced response to sea ice loss because the lower-latitude warming that occurs in a fully coupled experiment can in turn impact the midlatitude response. To better separate the tropically driven component of the component driven by sea ice loss, we use two-parameter pattern scaling (Blackport and Kushner 2017). This yields *pattern-scaled sensitivities* to low- and high-latitude drivers that are obscured by the cross-coupling in the coupled model responses. By cross-coupling, we mean, for example, that warming at low latitudes in the model in response to sea ice loss can induce a response in the extratropics.

a. Models and simulations

The MEs (i.e., the coupled models and experimental protocols) used in this study are presented in Table 1. For ease of reference to the previous literature, the nomenclature used in the original publications is included in the table (second column). Five models are listed (first column, and described below) with their approaches to isolating the response to sea ice loss from greenhouse warming (fourth and fifth column), which are also discussed in Screen et al. (2018) and Sun et al. (2020). Another key distinction between approaches is whether transient or equilibrated solutions are examined (sixth column). Each of the MEs provides a forced response that is dominated by sea ice loss or by the combined effects of both warming and sea ice loss, and some additionally provide a forced response dominated by warming with very little sea ice loss.

TABLE 1. Summary of individual simulations and MEs used in this study, including the nomenclature from the original publication, how many ensemble members and years of simulation we have, the radiative forcing and targeted ice area/volume, and whether the integrations are performed as transient or time-slice experiments. The symbols shown in the model column are the same as those used in Fig. 1. Superscript numbers after the simulation names indicate the references—1: Blackport and Kushner (2017), 2: Kay et al. (2015), 3: England et al. (2020b), 4: Marsh et al. (2013), 5: McCusker et al. (2017), 6: Oudar et al. (2017), and 7: Sun et al. (2018).

Model	Simulation name	No. members and years simulated	Radiative forcing	Ice target	Transient?
CESM1◇	Control[1]	1 × 735 years	Y2000	Unconstrained	No
	Low Albedo[1]	1 × 540 years	Y2000	Unconstrained	No
	Large Ensemble[2]	40 × 180 years	Historical/RCP8.5	Unconstrained	Yes
WACCM4○	CONTROL[3]	1 × 351 years	1955–69	1955–69	No
	ARCTIC[3]	1 × 351 years	1955–69	2085–99	No
	CMIP5[4]	3 × 145 years	Historical/RCP8.5	Unconstrained	Yes
CanESM2◁	$C_{PI}I_{PI}$[5]	1 × 201 years	1 × CO_2	1 × CO_2	No
	$C_{2X}I_{2X}$[5]	1 × 201 years	2 × CO_2	2 × CO_2	No
	$C_{2X}I_{PI}$[5]	1 × 300 years	2 × CO_2	1 × CO_2	No
	$C_{PI}I_{2X}$[5]	1 × 300 years	1 × CO_2	2 × CO_2	No
CNRM-CM5□	CTL20[6]	1 × 200 years	Late 20th	Late 20th	No
	CTL21[6]	1 × 200 years	Late 21st	Late 21st	No
	ICE21[6]	1 × 200 years	Late 21st	Late 20th	No
	ICE20[6]	1 × 200 years	Late 20th	Late 21st	No
GFDL CM3▷	RCP8.5[7]	5 × 120 years	RCP8.5	Unconstrained	Yes
	ICE1990[7]	5 × 100 years	RCP8.5	1990s	Yes

1) CESM1: The configuration of the Community Earth System Model, version 1 (CESM1), used for the CESM Large Ensemble (LENS) (Kay et al. 2015, and references therein), with a nominal resolution of 1° in both the atmosphere and the ocean, is used here. The forced sea ice loss response is obtained from the difference between multicentennial means of simulations outlined in Blackport and Kushner (2017). These consist of a control simulation with constant year-2000 forcing (branched from member 101 of the LENS simulations at nominal year 0) and a reduced sea ice simulation branched at year 301 from the control simulation, in which the albedo of the sea ice is permanently reduced globally. To obtain the forced response to external RCP8.5 forcing, dominated by greenhouse warming, we choose two 20-yr mean epochs from the 40-member ensemble mean of the CESM LENS simulations in which sea ice close matches that found in the control and perturbed albedo experiments.
2) WACCM4: The Whole Atmosphere Community Climate Model, version 4, provides improved stratospheric representation relative to the atmospheric component of CESM1, but uses previous versions of atmospheric physical parameterizations and a coarser nominal horizontal resolution of 2°. The ocean model is similar to CESM1 LENS, and the simulations are carried out at a nominal 1° ocean resolution. The CONTROL and ARCTIC simulations used here are described in England et al. (2020b). These are analogous to the simulations performed with CESM1 in that they consist of long simulations of which one has a high sea ice area and one has a reduced sea ice area, all else equal; however, they differ in length, the control climate state, and in the sea ice loss protocol. The longwave forcing method of Deser et al. (2015) is used to emulate the sea ice extent in the Arctic to the mid-twentieth century in CONTROL, and the end of the twenty-first century for ARCTIC. For each, the last 250 yr of a 350-yr simulation are retained for analysis. A small ensemble of three CMIP5 RCP8.5 simulations is used to describe projected greenhouse gas forcing in this model (Marsh et al. 2013).The 15-yr epochs chosen from the CMIP5 RCP8.5 WACCM simulations are those from which the sea ice targets for CONTROL and ARCTIC are taken.
3) CanESM2: These simulations, outlined in McCusker et al. (2017), use the second generation of the Canadian Earth System Model at spectral horizontal resolution T63. These MEs consists of four simulations in which the Arctic sea ice mass is nudged grid cell by grid cell to match that from equilibrated preindustrial CO_2 (I_{PI}) or 2 × CO_2 (I_{2X}) sea ice distributions of the free-running CanESM2 model. For each of these sea ice distributions, the radiative forcing is set to either preindustrial (PI) or 2 × CO_2 (2X), and the model is integrated for 201 yr for the two control simulations (i.e., those in which the target sea ice distribution is matched to the radiative forcing) and 301 yr for the two perturbed simulations, where the target sea ice distribution is mismatched with the radiative forcing. In each case, the last 200 yr are retained for analysis. The greenhouse warming–forced response is given by the difference between the two controls, $C_{2X}I_{2X}$ and $C_{PI}I_{PI}$, while the forced response to sea ice loss can be isolated at both cooler and warmer background climates by using the other two simulations. Additionally, the forced response to warming with very little ice loss at high or low ice cover can be explicitly determined for this ME, unlike for the CESM1 and WACCM4 MEs.
4) CNRM-CM5: These simulations are outlined in Oudar et al. (2017). The atmosphere and ocean components of this version of the model have a horizontal resolution of 1.4° and 1°, respectively. These MEs consist of four simulations that are analogous to those performed with

TABLE 2. A summary of the response pattern names used in this paper and how they are calculated, including the names of the simulations as they are in the original publication, as well as the time periods chosen here. The right two columns show the amount of annual mean low-latitude warming in degrees Celsius and Arctic sea ice loss in millions of kilometers squared between the differenced simulations. These are the values that are used to obtain the matrices used to calculate the sensitivities. The boldface responses are those that represent the response to Arctic sea ice loss in isolation in a cool background climate, whereas the italicized responses are those to both radiative forcing and sea ice loss. The symbols shown in the model column are the same as those used in Fig. 1.

Model	Response	δT (°C)	δI (10^6 km^2)
CESM1◇	*Large Ensemble = LENS(2057:2066) − LENS(2027:2036)*	1.16	2.27
	Albedo = Low Albedo(501:840) − Control(301:735)	0.35	2.30
WACCM4○	*WACCM-CMIP5 = CMIP5(2085:2099) − CMIP5(1955:1969)*	1.68	2.33
	WACCM-ARCTIC = ARCTIC(101:350) − CONTROL(101:350)	0.35	4.45
CanESM2◁	*Full = $C_{2X}I_{2X}$(2:201) − $C_{PI}I_{PI}$(2:201)*	2.27	4.43
	ICEcold = $\mathbf{C_{PI}I_{2X}}$(101:300) − $\mathbf{C_{PI}I_{PI}}$(2:201)	0.16	4.07
	ICEwarm = $C_{2X}I_{2X}$(2:201) − $C_{2X}I_{PI}$(101:300)	0.28	4.07
	CO2lo = $C_{2X}I_{2X}$(2:201) − $C_{PI}I_{2X}$(101:300)	2.12	0.36
	CO2hi = $C_{2X}I_{PI}$(101:300) − $C_{PI}I_{PI}$(2:201)	2.00	0.36
CNRM-CM5□	*ICE+GHG = CTL21(101:200) − CTL20(101:200)*	2.64	7.10
	ICE Effect 21 = ICE20(101:200) − CTL20(101:200)	0.12	6.55
	ICE Effect 20 = CTL21(101:200) − ICE21(101:200)	0.34	6.39
	GHG Effect 20 = ICE21(101:200) − CTL20(101:200)	2.30	0.7
	GHG Effect 21 = CTL21(101:200) − ICE20(101:200)	2.52	0.55
GFDL CM3▷	*ΔRCP8.5 = RCP8.5(2070:2090) − RCP8.5(1990:2010)*	2.04	6.02
	ΔICE1990 = ICE1990(2070:2090) − ICE1990(1990:2010)	01.83	0.2
	ΔICE = [RCP8.5(2070:2090) − RCP8.5(1990:2010)] − [ICE1990(2070:2090) − ICE1990(1990:2010)]	0.21	5.82

CanESM2: they utilize a non-solar flux correction to the ocean model to control the seasonal cycle of Arctic sea ice to match that from the late twentieth or late twenty-first century resulting from historical or RCP8.5 radiative forcing, while the radiative forcing itself is set to either the late twentieth century or late twenty-first century. Each integration is 200 yr in length, and the last 100 yr are retained for analysis. Again, this experimental design allows us to also explicitly assess the forced response to greenhouse warming with very little sea ice loss.

5) GFDL CM3: Version 3 of the Geophysical Fluid Dynamics Laboratory Coupled Model has an atmospheric resolution of approximately 200 km, while the ocean component has a latitudinal resolution of 1° and enhanced longitudinal resolution reaching 1/3° near the equator. The experiments outlined here are those of Sun et al. (2018): five ensemble members of an integration representing 1970–2090 in which ice is unconstrained and radiative forcing is given by historical and RCP8.5 forcing provides the forced response to greenhouse warming. Another experiment of five ensemble members is also carried out whereby ice is constrained using a volume-nudging method similar to the mass-nudging method of McCusker et al. (2017) to match its mean distribution from 1970 to 1990. This experiment is integrated from 1990 to 2090 to provide the transient response to RCP8.5 radiative forcing with very little sea ice loss. The difference between the ensemble means then gives the transient forced response to sea ice loss.

The way the forced responses are diagnosed from the MEs are shown in Table 2, retaining the nomenclature from the original publications. We separately group the simulations that are run to equilibrium with unchanging sea ice and radiative forcing and those that are integrated with transient forcing. We plot annual mean Arctic sea ice area versus low-latitude sea surface temperature (area-weighted average over 0°–40°N) in Figs. 1a and 1b. The transient simulations in Fig. 1b show 15-yr running means as well as the periods chosen in determining the forced response. Each response that we diagnose is then shown in Fig. 1c on a plot of Arctic sea ice loss and low-latitude warming, where the responses are color-coordinated to distinguish between the three types of forced responses: warming under near-constant sea ice area, for which 2.0°–3.0°C of low-latitude warming is obtained with less than 1 million km^2 of Arctic sea ice loss; sea ice loss under near-constant low-latitude warming, for which less than 0.5°C of low-latitude warming is obtained with 3.0–8.0 million km^2 of sea ice loss; and full greenhouse warming, for which about 1°C of low-latitude warming is obtained per 2 million km^2 of Arctic sea ice loss.

b. Pattern scaling

There is no consistent framework upon which these MEs are designed and as a result there are differing amounts and patterns of sea ice loss and ocean, atmospheric, and land warming. For example, we show, for each season, the sea ice fraction in each ME's low sea ice simulation relative to the 15% sea ice extent contour in its control simulation in Fig. 2. This figure highlights the disparate patterns and magnitudes of sea ice loss across the MEs considered in this study, motivating the need to normalize the forced responses before a

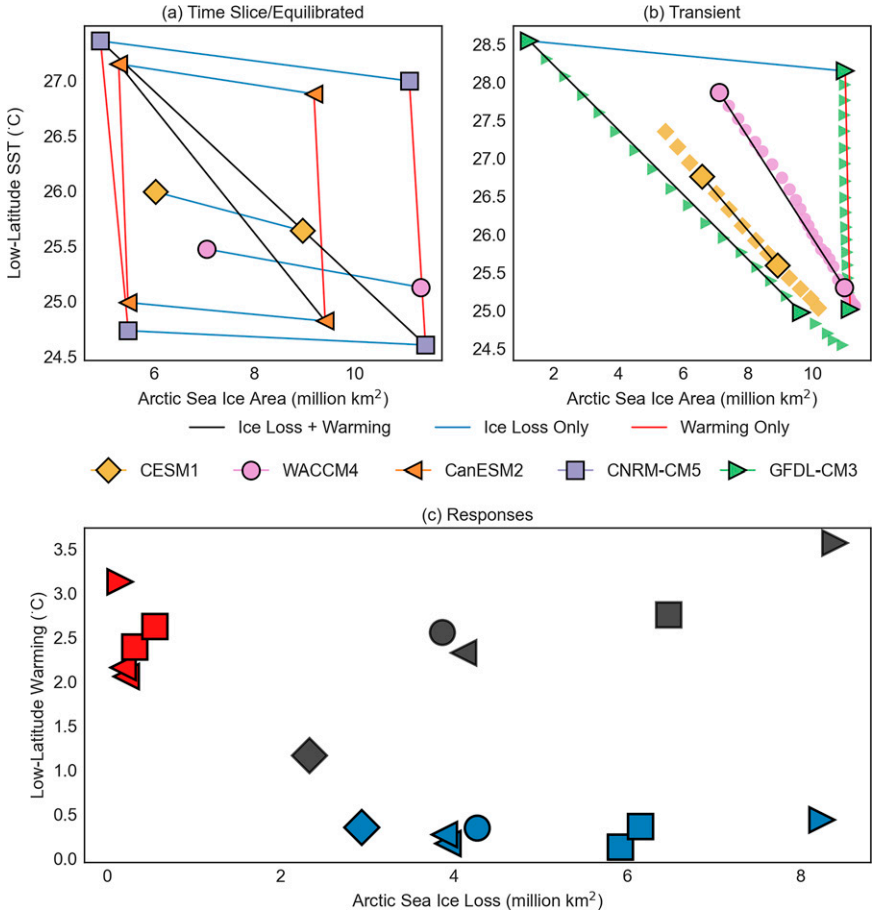

FIG. 1. (a) The amount of annual-mean Arctic sea ice and Northern Hemisphere low-latitude (0°–40°N) SST for each of the time slice or equilibrated simulations, as indicated in Table 1. (b) As in (a), but for the transient experiments. For these, we also show the evolution in time for each 15-yr epoch of each simulation, with the time periods chosen for analysis (see Table 2) outlined in black. The models are color- and shape-coded according to the legend, and the colors of the lines connecting the various simulations indicate what response (ice loss alone, warming alone, or both ice loss and warming together) was obtained by differencing those specific simulations. (c) The amount of Arctic sea ice loss and low-latitude warming in these various responses. The shape of the symbol corresponds to the model, and the color of the symbol groups the responses according to the type of response.

comparison can be made. The study by McCusker et al. (2017) demonstrated the separability and linear additivity of the atmospheric response to sea ice loss and the rest of the greenhouse warming response. At the same time, the study of Blackport and Kushner (2017) introduced two-parameter pattern scaling to separate the sensitivity to LLW from that of sea ice loss. We use the same method here to address the inconsistencies in the MEs and their forced responses arising from differences in experimental design. This linear decomposition removes the signal of LLW from the pattern-scaled sensitivity to SIL, thus yielding the direct sensitivity to SIL while accounting for the cross-coupling from LLW. It yields also a direct sensitivity to LLW by removing the signal of SIL. Besides attempting to consistently scale for the amount of Arctic sea ice loss, pattern scaling also seeks to simultaneously scale for differences in tropical warming responses that might arise from radiative feedbacks (e.g., in the case of the CESM1 albedo reduction ME due to the additional effects of Antarctic sea ice loss on the tropics; England et al. 2020a).

The method of Blackport and Kushner (2017) has previously been used in Hay et al. (2018) to compare near-surface atmospheric sensitivities in two models, and in Feldl et al. (2020) to understand the locally and remotely driven components of the high-latitude lapse-rate feedback. Classically, pattern scaling simply states that the pattern of forced response to greenhouse warming in climate models is proportional to the global mean temperature (Santer et al. 1990; Tebaldi and Arblaster 2014; Bichet et al. 2015) and is independent of the details of the forcing. From the empirical observation that

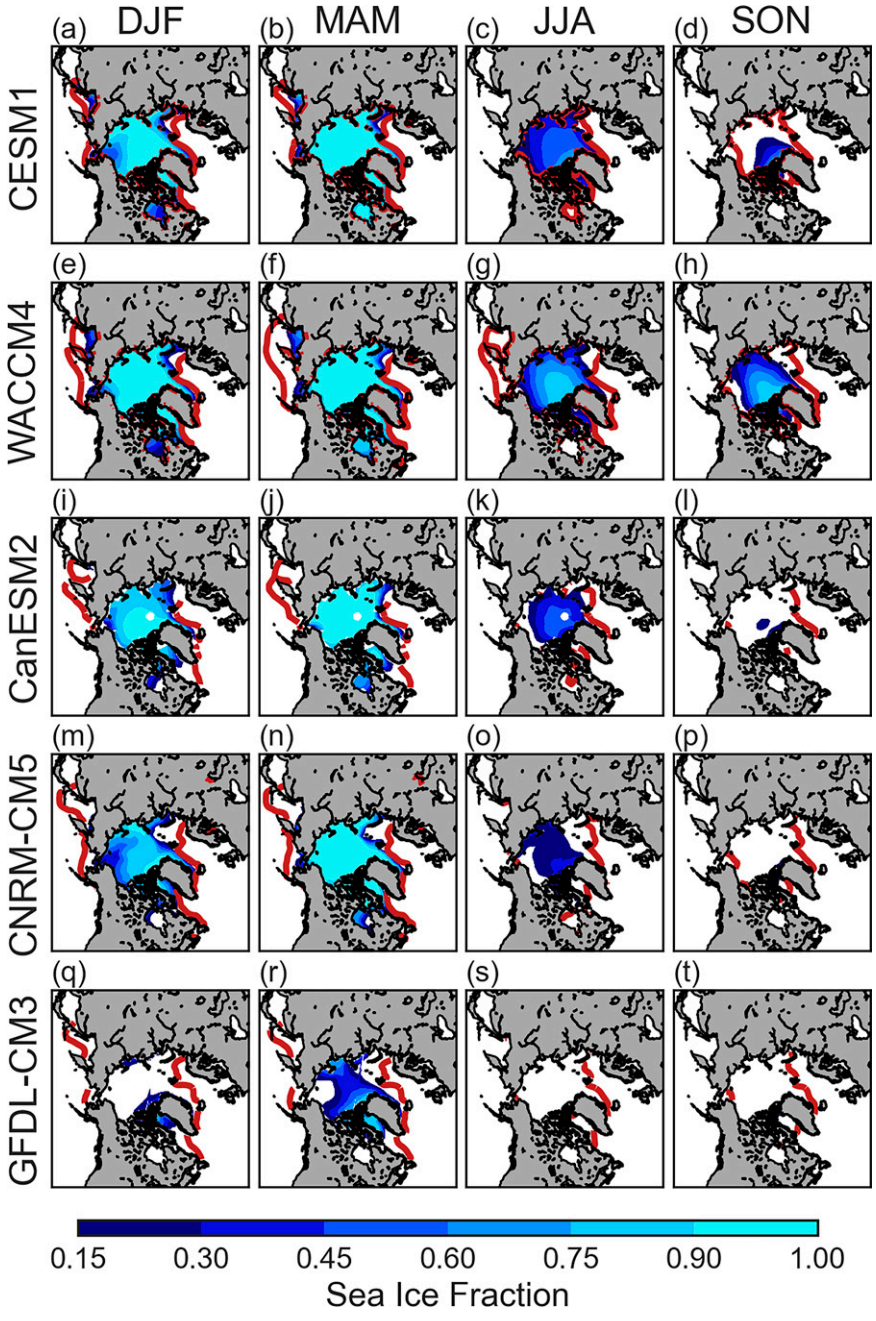

FIG. 2. The 15% contour of Arctic sea ice concentration in the control simulation (thick red contour) and the sea ice fraction in the simulation with low sea ice area (filled contours) for the (a)–(d) CESM1 MEs and the analogous (e)–(h) WACCM4, (i)–(l) CanESM2, (m)–(p) CNRM-CM5, and (q)–(t) GFDL CM3 MEs in (left) DJF, (left center) MAM, (right center) JJA, and (right) SON.

the zonal-mean temperature pattern response to sea ice loss resembles that from greenhouse forcing [the "mini-global warming" of Deser et al. (2015)], Blackport and Kushner (2017) generalized pattern scaling to multiple scaling variables. As in previous studies (Hay et al. 2018; Feldl et al. 2020) we use low-latitude (0°–40°N) sea surface temperature T_l and Arctic sea ice area I as the scaling variables. The forced response δZ_m of some variable Z for ME response m (i.e., the difference between two MEs in a given model) can be written as the sum of two patterns, one that is proportional to SIL and another that is proportional to LLW:

$$\delta Z_m = \left.\frac{\partial Z}{\partial I}\right|_{T_l} \delta I_m + \left.\frac{\partial Z}{\partial T_l}\right|_{I} \delta T_{l,m}. \quad (1)$$

The partial derivative terms represent the pattern-scaled sensitivities, and these can be determined provided at least two ME responses (i.e., $m \geq 2$) are available that feature linearly independent responses in LLW and SIL. Therefore, for a given set of MEs and a given season, we choose two forced responses and invert Eq. (1), solving for the sensitivities $\left.(\partial Z/\partial I)\right|_{T_l}$ and $\left.(\partial Z/\partial T_l)\right|_{I}$. These sensitivities are interpreted as an estimate of how Z would change if SIL hypothetically occurred with low-latitude temperatures held fixed and if LLW hypothetically occurred with sea ice held fixed. They are further interpreted as characterizing the forced model response, independent of the experimental protocols in the original MEs.

A related method of classical pattern scaling using linear least squares regression to determine the scaling relationship is less susceptible to slight nonlinearities (Mitchell 2003) and offers the advantage of the calculation of a residual term. However, this method is more computationally expensive (Herger et al. 2015), there are not many statistically significant differences in the methods found across CMIP5 models, and the regression method is more susceptible to differences in forcing scenario (Lynch et al. 2016). Analogous to the linear least squares method used in classical pattern scaling, an alternative approach to the one we use here may be constructed using multiple linear regression instead.

Pattern scaling as outlined here relies on the additivity of internal and external climate forcings. Within studies of detection and attribution of climate change, it is generally implicitly assumed that climate responses to external forcings (e.g., CO_2, anthropogenic aerosols, ozone, volcanic eruptions, and land use changes) can be linearly added to obtain the total climate response to the sum of the forcings (Stott et al. 2010). This assumption has been tested in a number of studies and it has been found that temperature is generally additive under all scenarios, but additivity breaks down in other fields such as precipitation under some forcing scenarios (Shiogama et al. 2013; Marvel et al. 2015). Other studies have found significant nonlinearities in some seasons and regions (Deng et al. 2020). On the other hand, the additivity of the climate response to internal forcing agents, such as sea ice area and low-latitude temperature, as we have chosen to do here, has been studied less extensively, although there is evidence to support it (McCusker et al. 2017; Oudar et al. 2017). We can expect to obtain the best results from this method as long as we remain within in a linear regime and have sufficient sampling. It is important to note that the sensitivities as defined here do not necessarily imply causality; instead, that is what we get from the model responses. The pattern-scaled sensitivities are a way to further decompose the forced responses to reveal what is shared among the MEs, irrespective of their differences in experimental construction and sea ice loss protocols.

The two-parameter method is demonstrated in Fig. 3 for the decomposition of the forced zonal-mean temperature response in boreal winter in CNRM-CM5, using the nomenclature of Oudar et al. (2017). Five forced response patterns for this ME are shown: in Fig. 3a, ICE+GHG, which is the response to greenhouse warming; in Fig. 3b, GHG Effect 21, the response to greenhouse warming at fixed late-twentieth-century ice cover; in Fig. 3d, ICE Effect 20, the response to sea ice loss under late-twentieth-century greenhouse gas (GHG) concentrations; in Fig. 3f, GHG Effect 20, the response to greenhouse warming at late-twenty-first-century ice cover; and in Fig. 3h, ICE Effect 21, the response to sea ice loss under late-twenty-first-century GHG concentrations. Figure 3a shows the usual pattern of projected greenhouse warming with an overall warming of the troposphere at all Northern Hemisphere latitudes with amplified warming in the Arctic lower troposphere and in the tropical upper troposphere, alongside cooling in the stratosphere. In Figs. 3b and 3f, when GHG forcing is applied with sea ice held fixed, the pattern closely resembles that in Fig. 3a but it lacks surface Arctic amplification and instead shows Arctic warming with a weak maximum in the midtroposphere. Interestingly, in Fig. 3f, there is a hint that greenhouse gas radiative forcing under prescribed high ice conditions gives rise to surface cooling, something that was found after the pattern-scaling decomposition for CESM1 in Hay et al. (2018). This weak but significant cooling response to GHG forcing with fixed ice cover may arise as an artifact of the sea ice nudging. In Figs. 3d and 3h, when ice loss alone is imposed, an Arctic amplification pattern is seen, alongside a small amount of warming in the tropical midtroposphere, particularly in ICE Effect 21.

After the pattern-scaling decomposition we obtain the pattern-scaled sensitivities of this ME to LLW, $(\partial T^{\mathrm{zon}}/\partial T_l)|_I$, for each background climate in Figs. 3c and 3g and the pattern-scaled sensitivities to SIL, $(\partial T^{\mathrm{zon}}/\partial I)|_{T_l}$, for each background climate in Figs. 3e and 3i. We note the similarities of the sensitivities between background climates. Pattern scaling has removed the midtropospheric tropical warming seen in Fig. 3h from the modeled sea ice loss response pattern, and the Arctic amplification is slightly shallower, suggesting that some Arctic midtropospheric warming scales with LLW. The sensitivity to LLW comprises all the tropical warming as well as warming of the midtroposphere in the Arctic, with cooling found both at the surface and in the stratosphere. Because the stratospheric response to climate change is dominated by direct CO_2 radiative forcing, a process that is not at play in simulations forced by sea ice loss even with low-latitude warming, caution is required in interpreting sensitivities there. The amount of warming that occurs near the Arctic surface in Fig. 3b or Fig. 3h is greater than that in Fig. 3a, so it appears that in certain models a modest negative feedback near the Arctic surface arises—that is, a minimum in surface warming or even a cooling—which scales with LLW.

3. Results

a. Patterns of atmospheric sensitivity

We first extend the analysis of Hay et al. (2018), which included the same pattern-scaling decomposition for two of the MEs considered here, CESM1 and CanESM2, to include

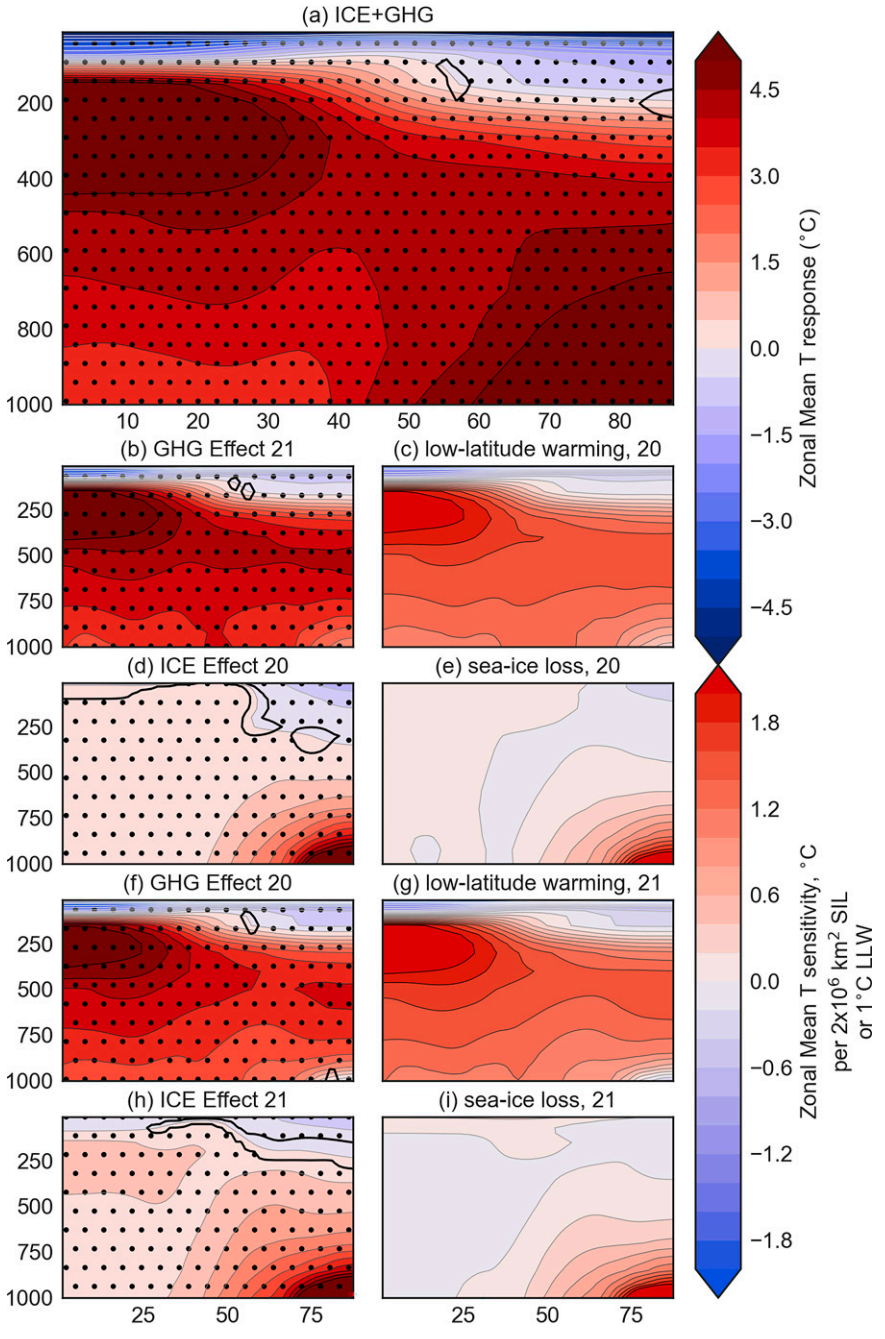

FIG. 3. An example of the pattern-scaling decomposition for zonal-mean temperature using all of the CNRM-CM5 ME simulations in DJF, showing (a) the ICE+GHG response and the (b) GHG Effect 21, (d) ICE Effect 20, (f) GHG Effect 20, and (h) ICE Effect 21 responses, δT_m^{zon}. Also shown are the patterns of sensitivity to (c) LLW, $\left(\partial T^{\text{zon}}/\partial T_l\right)\Big|_I$, per degree of warming and (c) SIL, $\left(\partial T^{\text{zon}}/\partial I\right)\Big|_{T_l}$, per 2 million km^2 of sea ice loss, utilizing the response patterns in (a) and (b) or (d). (g),(i) As in (c) and (e), but for the calculation utilizing the response patterns in (a) and (f) or (h).

more MEs and zonal-mean climate variables as well as the near-surface variables investigated in that study.

The left-hand column of Fig. 4 presents the mean boreal winter [December–February (DJF)] map of the sensitivity to Arctic SIL, per two million km^2 of ice loss, for surface temperature, sea level pressure, precipitation, and 850-hPa zonal wind for all MEs, while Fig. 5 shows the same for zonal-mean zonal wind and zonal-mean temperature. The right-hand

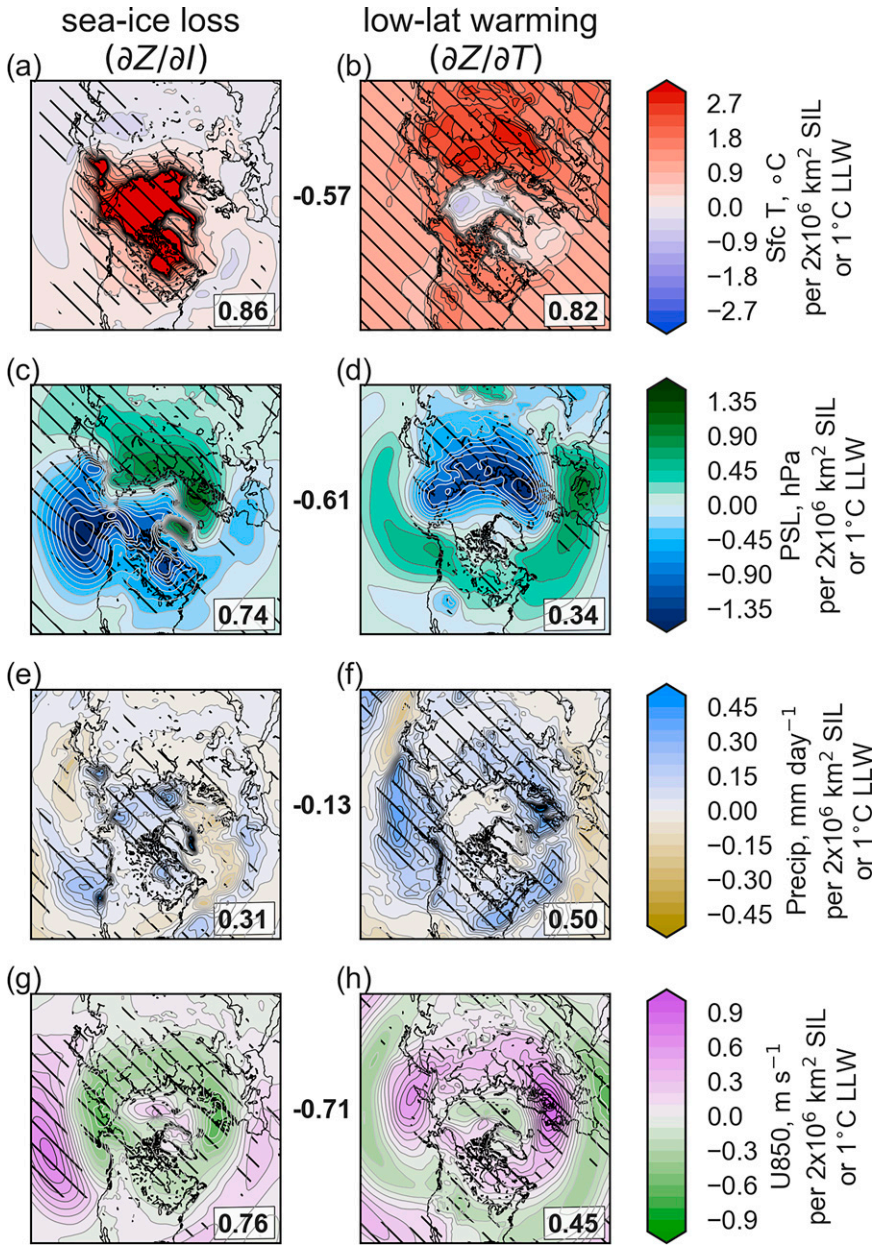

FIG. 4. The DJF multi-ME mean of the pattern of sensitivity to (left) SIL, $\left(\overline{\partial Z}/\partial I\right)\Big|_{T_l}$, per 2 million km^2 of Arctic sea ice loss and (right) LLW, $\left(\overline{\partial Z}/\partial T_l\right)\Big|_{I}$, per degree of warming for (a),(b) surface temperature; (c),(d) sea level pressure; (e),(f) precipitation; and (g),(h) 850-hPa zonal wind. In each panel, the hatched areas represent locations where at least four of the five MEs agree on the sign. The number in the lower-right of each panel represents the median pattern correlation across the different MEs, and the numbers between pairs of panels represent the pattern correlation between the mean sensitivity patterns.

column of Figs. 4 and 5 shows the sensitivity to LLW, per degree of warming. Scaling per 2 million km^2 of ice loss and per degree of warming arises from the observation that these models show roughly 1°C of tropical warming per 2 million km^2 of sea ice loss in response to greenhouse warming (Fig. 1). To obtain Figs. 4 and 5, we perform the pattern-scaling decomposition for each ME using the bolded and italicized combinations in Table 2. This results in patterns for each of the sensitivities and for each of the MEs. These patterns are then regridded onto a 1° by 1° global grid and averaged across the set of MEs. The hatched areas in Figs. 4 and 5 represent those regions where at least four of the five models agree

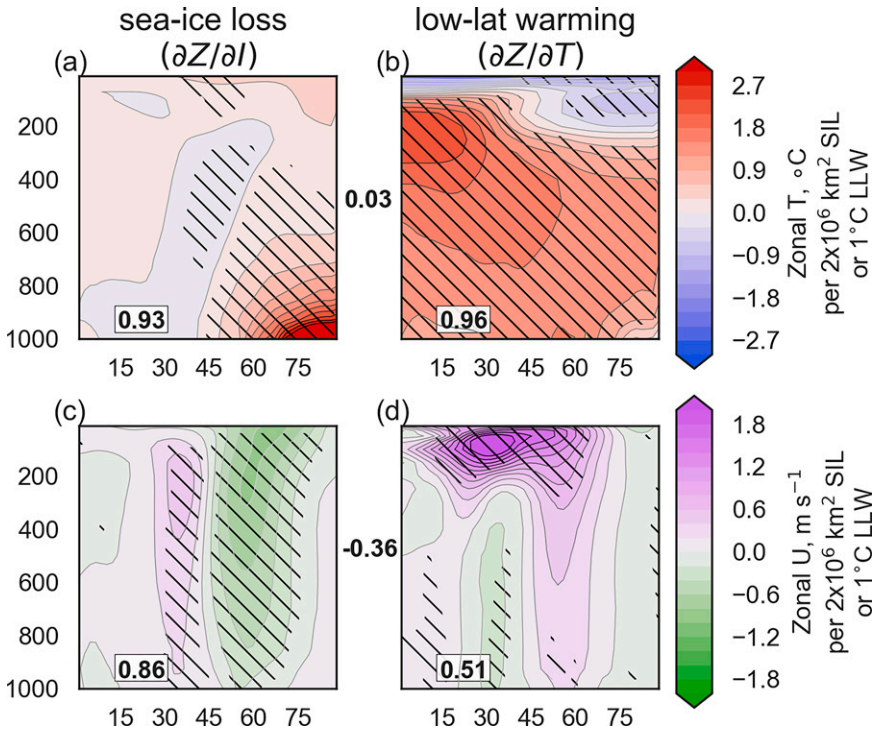

FIG. 5. As in Fig. 4, but for DJF zonal-mean (a),(b) temperature and (c),(d) zonal wind.

on the sign of the pattern-scaled sensitivity, and the number in the bottom right-hand corner indicates the median spatial correlation of all MEs with each of the rest of the set for the Northern Hemisphere extratropics (defined here to include all regions north of 30°N). The number between panels indicates the spatial correlation between the mean sensitivity to SIL and to LLW. A more negative number indicates that the sensitivity to SIL acts as a negative feedback on the sensitivity to LLW.

For comparison of how the pattern-scaled sensitivities differ from their forced response counterparts, Fig. 6 shows the same variables shown in Figs. 4 and 5 response to sea ice loss in the upper row, response to greenhouse warming with fixed sea ice (for the models that provide this) in the middle row, and response to greenhouse warming with freely evolving sea ice in the lower row.

The surface temperature sensitivity to Arctic SIL in DJF, shown in Fig. 4a, consists of a strong warming directly over the Arctic Ocean and Hudson Bay of more than 2°C per million km^2 of ice loss, as well as a more modest warming over adjacent high-latitude land areas and over the midlatitudes of North America. A weak cooling over eastern Eurasia is seen in the multimodel mean, but it is not robust except for a region of eastern China and Japan. As compared with the forced response shown in Fig. 6, pattern scaling implies that much of the midlatitude warming seen in the sea ice loss experiments can be attributed to the back effect of LLW and not directly to SIL.

The surface temperature sensitivity to LLW (Fig. 4b) correlates negatively with that the sensitivity to SIL ($r = -0.57$) and consists of a robust warming everywhere south of the Arctic Circle, excluding the subpolar North Atlantic Ocean. There is enhanced warming over Siberia and the Rocky Mountains. The temperature sensitivity over the Arctic is not robust, with three of the five models showing some cooling, as was seen in the zonal-mean temperature sensitivity to LLW in CNRM-CM5 in Fig. 3c. We note that there is little consistency over the subpolar North Atlantic in either of the two pattern-scaled sensitivities. This region also does not show a robust sign in the modeled responses (i.e., before we scale the patterns) to greenhouse warming, warming without ice loss, or sea ice loss (Figs. 6a,g,m). This lack of consistency appears to at least partially be related to intermodel differences in the location of the North Atlantic warming hole, differences that are reflected in the ocean response below.

To obtain a more complete picture of the robustness across MEs, Fig. 7 presents each of the inter-ME spatial correlations for all the seasons and the annual mean. The result is a distribution of inter-ME correlations for the sensitivities to SIL and LLW in blue and orange, respectively. The black bars represent the median of the correlations. A cluster of dots near $r = 1.0$ implies that all MEs agree on the pattern-scaled sensitivity, a large spread in dots implies that some MEs are highly correlated with one another while some are not (or are anticorrelated), and a clustering of dots near a lower r implies that the pattern-scaled sensitivities are not robust.

The spatial correlations in Fig. 7a show that the extratropical surface temperature sensitivities to both SIL and LLW are robust throughout the year except in boreal summer, when correlations between sensitivities to SIL are at a minimum. We expect that the sensitivity to SIL will be most robust in DJF (Hay et al. 2018; Screen and Blackport 2019a) due to the

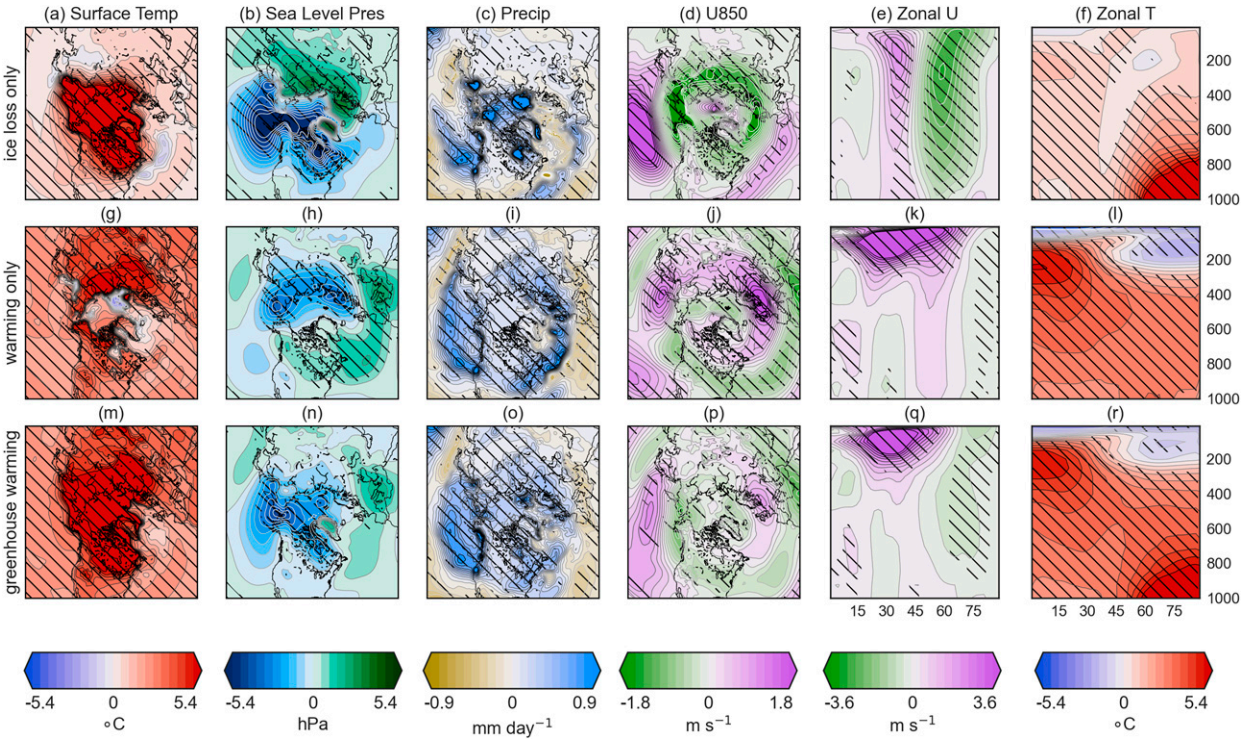

FIG. 6. The DJF modeled response to sea ice loss in DJF for (a) surface temperature, (b) sea level pressure, (c) precipitation, (d) 850-hPa zonal wind, (e) zonal-mean zonal wind, and (f) zonal-mean temperature. (g)–(l) As in (a)–(f), but for the response to warming alone. (m)–(r) As in (a)–(f), but for the response to greenhouse warming.

greatest turbulent heat fluxes in response to sea ice loss occurring then, despite having the largest ice losses in late summer and early autumn (Deser et al. 2010). Consequently, sea ice loss forcing in June–August (JJA) is weaker than in DJF and there is less consistency in forced model responses and pattern-scaled sensitivities. We note that the larger differences in sea ice area shown in Fig. 2 in JJA, with one ME nearly completely ice-free, may also be a confounding factor in the sensitivity comparison in this season.

The sea level pressure sensitivities are shown in Figs. 4c and 4d, and the forced responses in Figs. 6b and 6h. The pattern-scaled sensitivities are found to have opposite sign across most regions, with a correlation of $r = -0.61$, suggesting that sea ice loss response acts as a negative feedback on the sea level pressure response arising from the tropics. A robust sensitivity to SIL emerges with a deepening of the Aleutian low and lowered pressure from the Canadian Basin to Hudson Bay, alongside strengthening of the Siberian high. The latter pattern in forced atmosphere-only modeling studies has been associated with sea ice loss in the Barents and Kara Seas (Mori et al. 2014), but whether the same dynamical mechanism is at play in coupled modeling studies remains an open question. There is less consistency in the latitudinal extent of the Aleutian low, which contributes to some of the spread in correlations in Fig. 7b. Differences in the forced Aleutian low response were attributed to differences in tropical precipitation between fully coupled and slab ocean sea ice loss responses in the same model Deser et al. (2016), which may indeed be the case here, as the precipitation sensitivity to SIL can be seen in left-hand column Fig. 8 and we note little inter-ME agreement in the tropics.

The Siberian high sensitivity to LLW is a weakening with increasing temperature, and this weakening directly opposes the strengthening of the Siberian high associated with the warm-Arctic–cold-Eurasia (WACE) pattern (Mori et al. 2014). This regional tug-of-war suggests that changes to the Siberian high associated with the WACE pattern would be difficult to observe in a warming world in the presence of both tropical and Arctic warming. Apart from this signal, the entirety of the Western Hemisphere's sensitivity pattern is not robust to LLW. The Aleutian low either deepens or weakens depending on the ME in question, as was seen in Hay et al. (2018), and this is the reason for the negative pattern correlations seen in DJF in Fig. 7b. The pattern-scaled sensitivities in the Atlantic sector are not particularly robust to either forcing.

There is a large spread in the inter-ME correlations of LLW pattern-scaled sensitivities in DJF, and to a lesser extent in the other seasons, and the largest spread in correlations between the SIL sensitivities is in JJA. We find, as in the surface temperature sensitivity, that the most robust sensitivity to LLW occurs in JJA, which is the same season for which we find the least robust sensitivity to SIL, as indicated by the median in correlations.

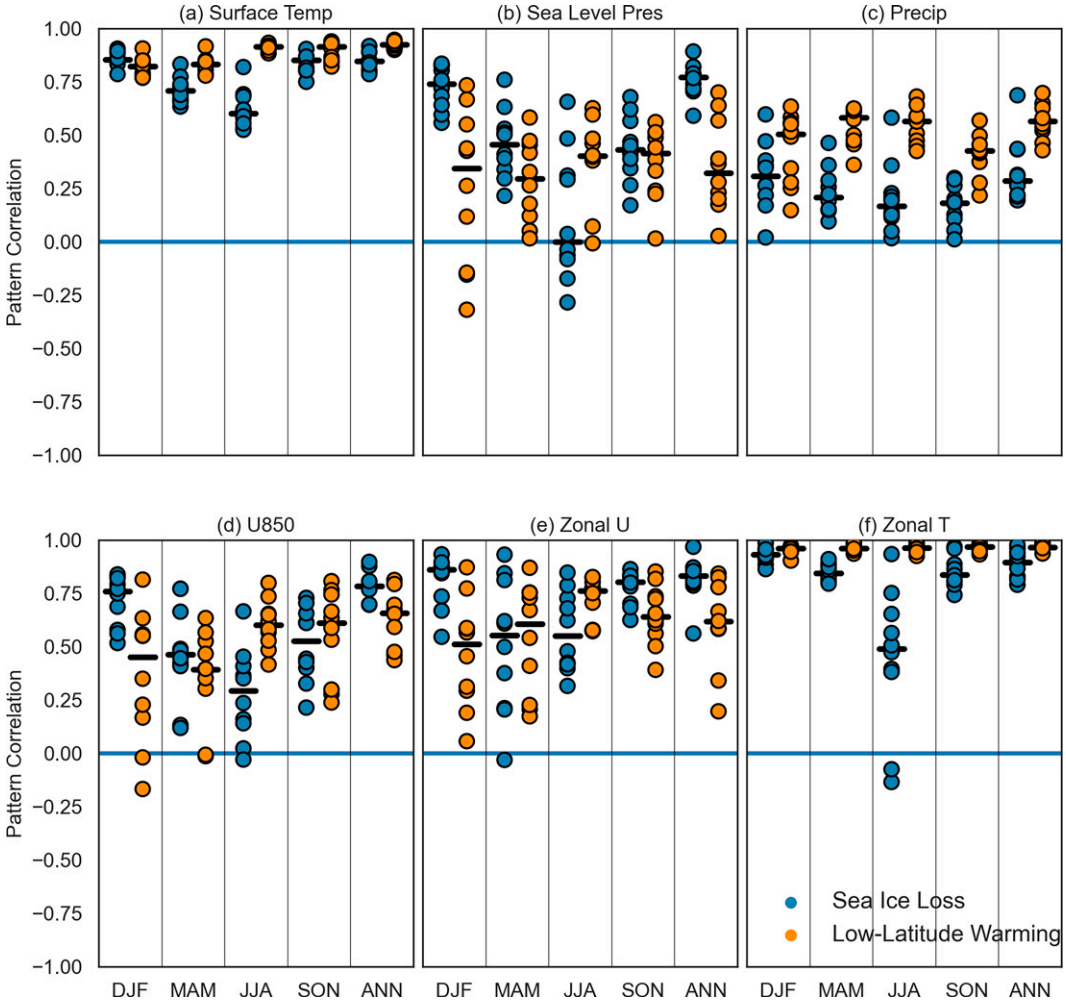

FIG. 7. Pattern correlations over the Northern Hemisphere extratropics (defined as all regions north of 30°N), with each dot representing the inter-ME correlation between individual sensitivity patterns, of (a) surface temperature, (b) sea level pressure, (c) precipitation, (d) 850-hPa zonal wind, (e) zonal-mean zonal wind, and (f) zonal-mean temperature obtained through pattern scaling for each season (DJF, MAM, JJA, and SON) as well as in the annual mean (ANN). The blue dots represent correlations between the SIL sensitivity patterns, and the orange dots represent correlations between the LLW sensitivity patterns. The black horizontal bars represent the median of the correlations.

The precipitation pattern-scaled sensitivities are shown in Figs. 4e and 4f and in Fig. 8, and the forced responses are shown in Figs. 6c, 6i, and 6o. Although the sensitivities are highly structured, pattern scaling helps to normalize and remove some of the noise from the responses over the Arctic Ocean. There are regions of consistently signed sensitivities to both SIL and to LLW. The global precipitation sensitivities for individual models (Fig. 8) shows the consistency in SIL (left-hand column) sensitivities is confined to the higher-latitude northern extratropics, while the consistency in LLW (right-hand column) sensitivities covers the midlatitudes and tropics of each hemisphere, in the annual mean. In Fig. 4e and in each individual model in Fig. 8, an increase in precipitation over the Arctic Ocean is seen as a result of increased evaporation from the ocean surface under SIL (Bintanja and Selten 2014). Additionally, consistent with the strengthening of the Aleutian low and the inter-ME spread in that pattern-scaled sensitivity, an increase in precipitation on the western coast of North America is seen. However, its exact latitudinal position is dependent on the ME. In Fig. 4f, the sensitivity to LLW shows a robust increase of precipitation over much of the midlatitudes, including western Europe, northern Eurasia, and both coasts of North America, and a drying over the subtropical eastern Atlantic and the Mediterranean. We find that median spatial correlations are lower overall than they were for surface temperature and sea level pressure, ranging from $r = 0.1$ to $r = 0.5$ for each collection of sensitivities. The spatial correlations across MEs are generally greater for the sensitivity to LLW than to SIL (Fig. 7c).

The sensitivity to SIL of the 850-hPa zonal wind over the Pacific Ocean (Fig. 4g) is largely consistent with the sea level pressure sensitivity. This includes a general weakening on the

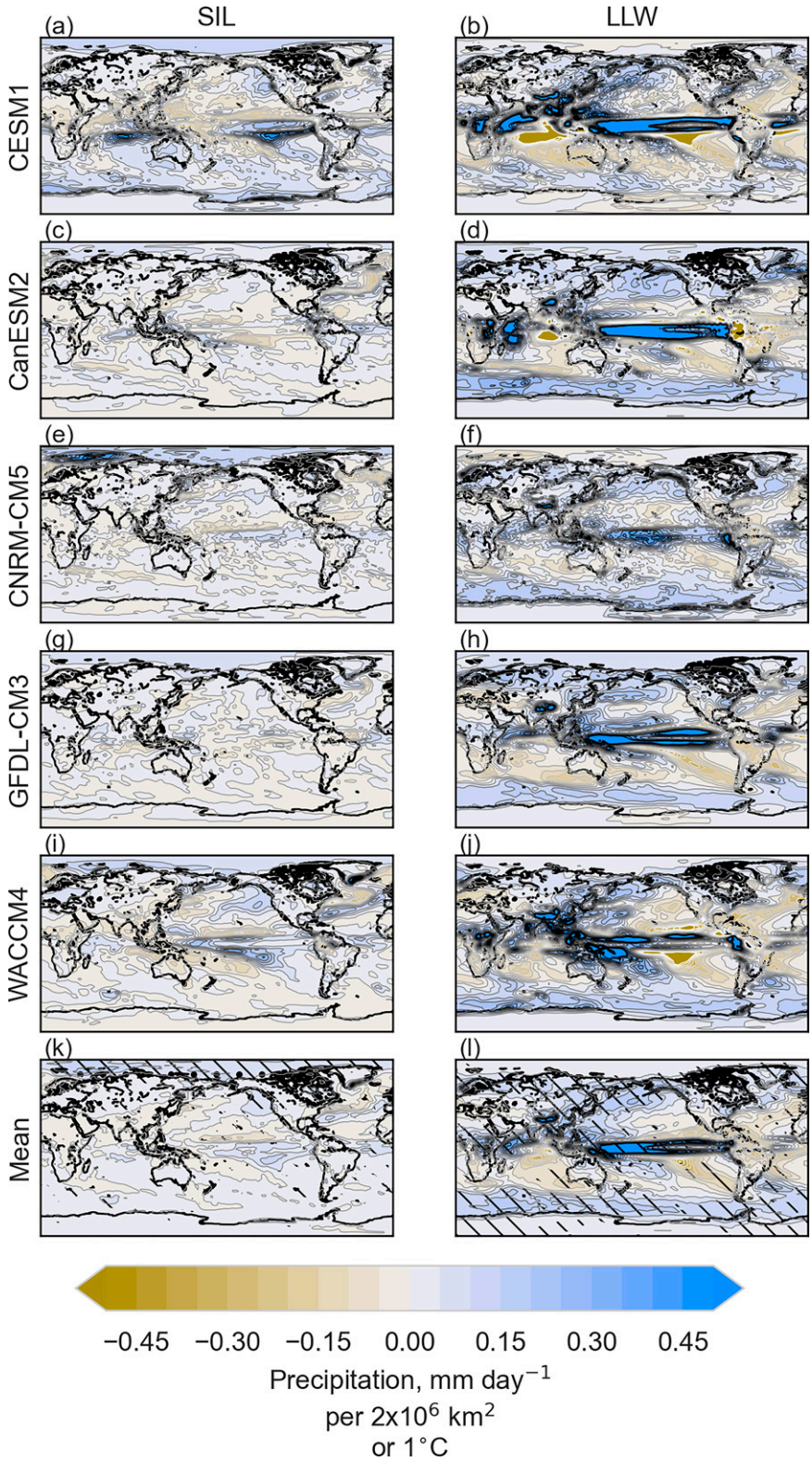

FIG. 8. The sensitivity of annual mean precipitation to (left) SIL and (right) LLW in (a),(b) CESM1; (c),(d) CanESM2; (e),(f) CNRM-CM5; (g),(h) GFDL CM3; and (i),(j) WACCM4. Also shown are the multi-ME mean sensitivity to (k) SIL and (l) LLW. Hatching represents where at least four of the five MEs agree on the sign of the sensitivity.

poleward flanks of the climatological maximum jet, indicating a southward shift in the Pacific storm track, as expected in response to a decrease in the equator to pole temperature gradient via the thermal wind relationship and under a reduction in baroclinicity. A similar pattern is seen in the Atlantic, and although it is not as robust in the pattern-scaled sensitivity or in the forced response (Fig. 6d), it resembles that found in Peings et al. (2019) for simulations dominated by the effects of Arctic amplification rather than upper tropospheric warming. In most seasons we see a large spread in correlations, and once again the median value of correlation is lowest in JJA. Looking at the sensitivity of zonal-mean zonal wind in a latitude–height cross section (Fig. 5c), a robust weakening and equatorward intensification is seen, consistent with the dominant pattern in U850. This is in agreement with other studies (Deser et al. 2015; Blackport and Kushner 2017).

The midlatitude U850 and tropospheric zonal-mean zonal wind sensitivity to LLW (Figs. 4h and 5d) is, on average, of opposite sign ($r = -0.71$ and $r = -0.36$, respectively) to the SIL sensitivity, so that LLW results in poleward intensification of the jet, as expected for an increase in the equator to pole temperature gradient aloft, and in good agreement with the idea of a "tug-of-war" between high- and low-latitude forcing (Harvey et al. 2014; Barnes and Screen 2015; Peings et al. 2019). The competing influences of high- and low-latitude forcing are seen in the forced responses in Figs. 6e and 6k. The mean pattern-scaled sensitivities reveal better intermodel agreement in the sensitivity to LLW, particularly at low levels, in the midlatitudes. This sensitivity is not robust in DJF at higher altitudes in the zonal mean, due to differences in the Atlantic and Pacific basins. The most robust part of the sensitivity to LLW is the strengthening of the subtropical jet.

Last, we examine the mean pattern-scaled sensitivities of zonal-mean temperature in Figs. 5a and 5b. The sensitivity to SIL is similar to Arctic amplification and is robustly seen in all models. The latitudinal and vertical extent of the warming is from 45°N to the pole and from the surface up to 400 hPa and is significantly reduced relative to the forced response in Fig. 6f. A weak but robust cooling in the midtroposphere and warming above 200 hPa in the midlatitudes is also found. The sensitivity to LLW is a robust warming throughout the troposphere, intensified at the tropical upper troposphere. In the Arctic lower troposphere we note again that the MEs disagree on the sign of the sensitivity. Stratospheric cooling of the Arctic is robustly associated with LLW, while the stratospheric sensitivity to SIL is not robust, in agreement with the indirect method of Screen and Blackport (2019a). Inter-ME spatial correlations in zonal-mean temperature are all closely clustered above $r = 0.8$ (Fig. 7f) except for the SIL sensitivities in JJA that have a large spread in correlations.

Overall, in DJF [and to a lesser extent in March–May (MAM), September–November (SON), and the full year (ANN)], the pattern-scaled atmospheric sensitivities to SIL are more consistent between MEs than to LLW, for the near-surface climate variables (surface temperature, sea level pressure, and 850-hPa zonal wind), as evidenced by the median of the correlations shown by the black bars in Fig. 7. This reverses in JJA when the sensitivity to LLW is more robust in all variables. Therefore, the conclusions from Hay et al. (2018) generally hold in this larger pool of models and sea ice loss protocols.

Before carrying out an analysis of the ocean's surface sensitivity, we decompose surface heat flux responses over the ocean (Fig. 9). The sign of the flux is defined to be positive upward into the atmosphere. The sensible heat flux sensitivity to SIL (Fig. 9a) is positive where sea ice is lost in the Arctic, and negative equatorward of the climatological sea ice margins. Robustness is confined to the Arctic Ocean itself, as well as a weak but robust positive heat flux south of the Kuroshio Extension. The former arises when sea ice is lost, exposing the ocean to the atmosphere and driving a greater transfer of heat from the ocean to atmosphere. Equatorward of the sea ice margin, atmospheric warming from SIL leads to anomalous warming of the ocean from downward heat fluxes (Deser et al. 2010). On the other hand, the latter result of upward sensible heat south of the Kuroshio is curious because the surface ocean (see Fig. 10 below) and overlying atmosphere (Fig. 4a) both exhibit cooling in the sensitivity to SIL in the same region. Inter-ME agreement in DJF is not as good as for some of the other surface variables, with the median $r = 0.48$. Here, the details in the differences of the patterns of sea ice loss (Fig. 2) may be driving the lower pattern correlation. Over the ocean, the sensible heat flux sensitivity to LLW (Fig. 9b) is downward everywhere, suggesting that the atmospheric warming of tropical origin consistently drives anomalous ocean warming throughout the Northern Hemisphere. While the inter-ME median r is similar, the sign of the sensitivity is robust nearly everywhere. The sensitivities are moderately negatively correlated with each other.

We find a similar pattern in the latent heat flux sensitivity to SIL (Fig. 9c), with an upward flux where sea ice is lost and downward flux equatorward of the sea ice loss region, but inter-ME agreement is somewhat weaker, with median $r = 0.36$. Regions of agreement are confined to higher latitudes in the sensitivity to SIL. On the other hand, the sensitivity to LLW (Fig. 9d) is robustly positive over all regions but the Arctic Ocean and the subpolar North Atlantic.

The longwave flux sensitivity to SIL (Fig. 9e) exhibits Arctic amplification, while the sensitivity to LLW (Fig. 9f) is a robust but weak negative signal that is likely associated with poleward heat and moisture transport (Lee et al. 2019).

Overall, in contrast to the atmospheric variables presented in Figs. 4 and 5, we find that, for surface fluxes, sensitivities to SIL are overall less robust than sensitivities to LLW. We can infer that the heat flux patterns are more strongly controlled by the pattern of sea ice loss, whereas the nature of the atmosphere depends less on the details of the sea ice loss. As in the atmosphere, there is a generally a negative correlation between the mean heat flux sensitivities to SIL and to LLW.

b. The ocean's sensitivity

The pattern-scaling decomposition (Hay et al. 2018), as well as other studies comparing the forced atmospheric response to sea ice loss in coupled models (Screen et al. 2018; Screen and Blackport 2019a), indicates that coupling to the

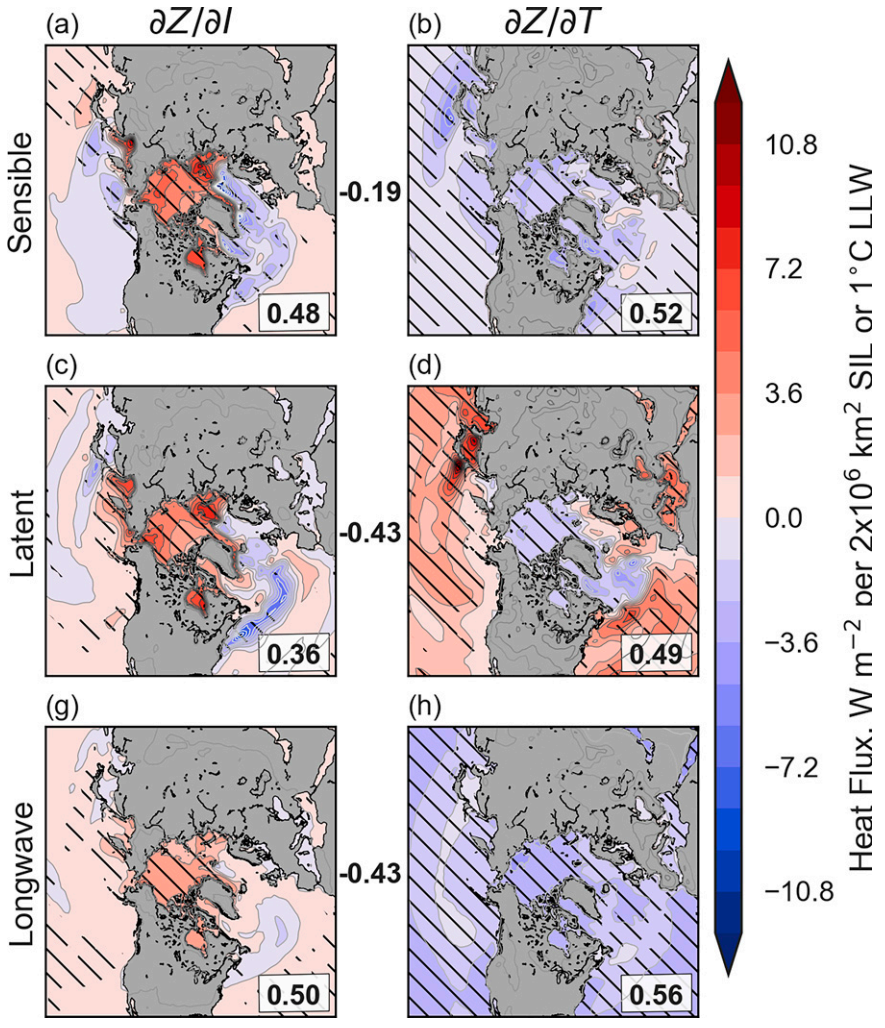

FIG. 9. As in Fig. 4, but for (a),(b) DJF sensible heat flux; (c),(d) latent heat flux; and (g),(h) surface net longwave flux. A flux from the ocean to the atmosphere is defined as positive.

ocean is important for the generating the sea ice loss response. To elucidate the role of the ocean, we decompose the forced surface ocean response using pattern scaling, as we did for the atmosphere. We present the results for sea surface temperature (SST) in Fig. 10 and for sea surface salinity (SSS) in Fig. 11. Because the greater inconsistency in the pattern-scaled sensitivities on regional scales relative to the atmosphere, we present not only the multi-ME mean as above, but also the individual MEs.

McCusker et al. (2017) demonstrated, with the CanESM2 MEs we use here, that there is separability and additivity of atmospheric responses to a doubling of CO_2 without sea ice loss and to Arctic sea ice loss under constant background CO_2. We have confirmed additivity in a second model by using the analogous CNRM-CM5 simulations for the atmospheric response. For example, McCusker et al. (2017) found that 98% of the surface temperature variability and 90% of the sea level pressure variability is explained by the sum of the sea ice loss and CO_2 forced responses, and in CNRM-CM5 we find the percentage of variability explained to be 99% for both surface temperature and sea level pressure. We applied the same analysis to the surface ocean and find that 79% of the SST variability and 92% of the SSS variability is explained by the sum of the forced responses in CanESM2, while in CNRM-CM5 the percentage of variability explained is 92% and 87%, respectively. These results justify the applicability of the linear pattern-scaling framework to our surface ocean analysis.

The sensitivity of annual mean SST to SIL for individual MEs and for the multi-ME mean, as shown in the left-hand column of Fig. 10 and in Fig. 10k, respectively, indicate that the ocean's surface warms robustly where sea ice is lost and solar radiation is absorbed by the ocean surface as well as where turbulent fluxes are in to the ocean (Figs. 9a,c). The pattern-scaled sensitivity in the Pacific presents as warming along the west coast of North America alongside a cooling that extends out across the western Pacific that resembles the positive phase of the PDO. This pattern is consistent with

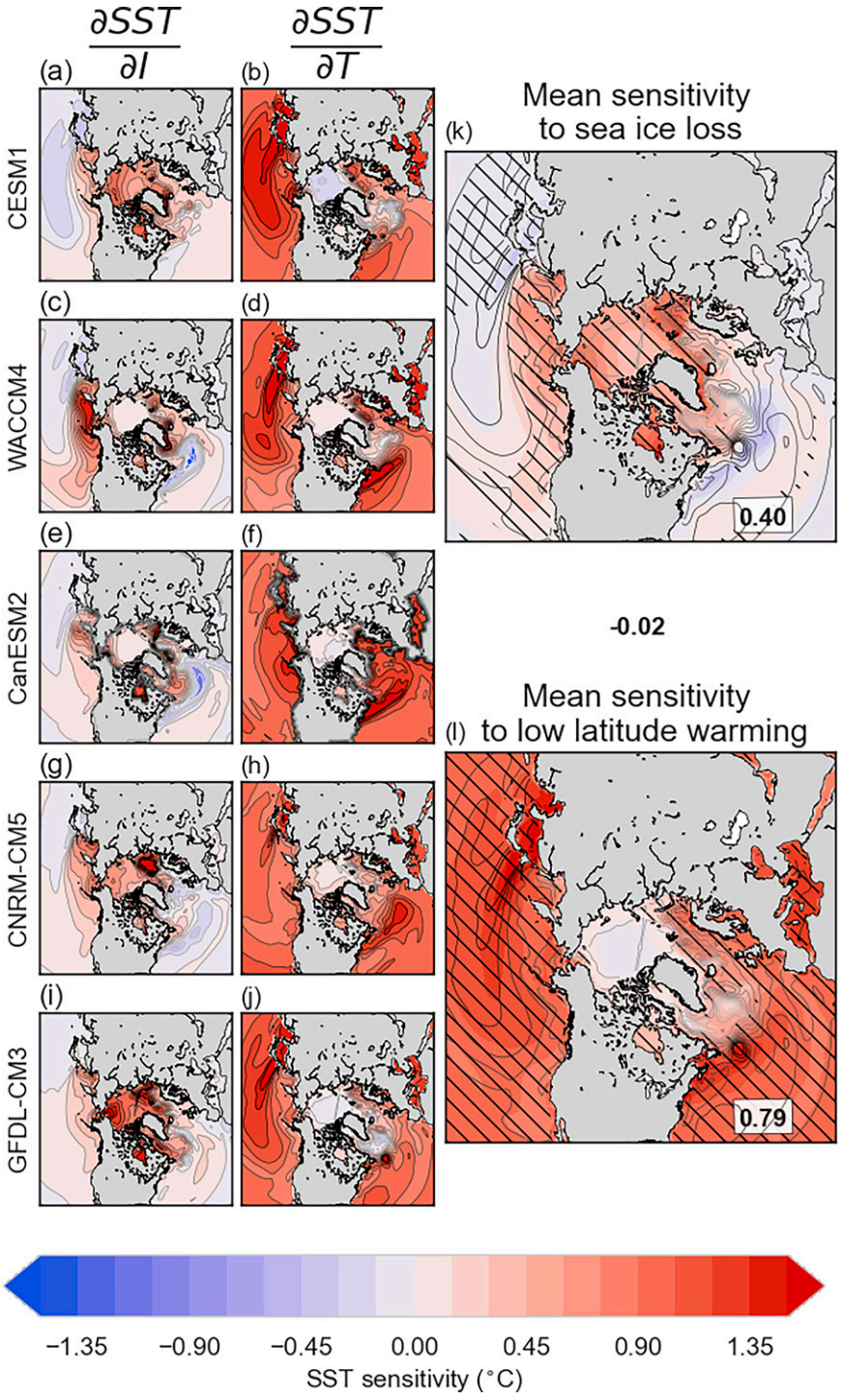

FIG. 10. The annual mean sensitivity of sea surface temperature to (left) Arctic SIL and (right) LLW for each of the MEs: (a),(b) CESM1; (c),(d) WACCM4; (e),(f) CanESM2; (g),(h) CNRM-CM5; and (i),(j) GFDL CM3 and for (k),(l) the multi-ME mean. The hatched regions represent where at least four of the five MEs agree on the sign.

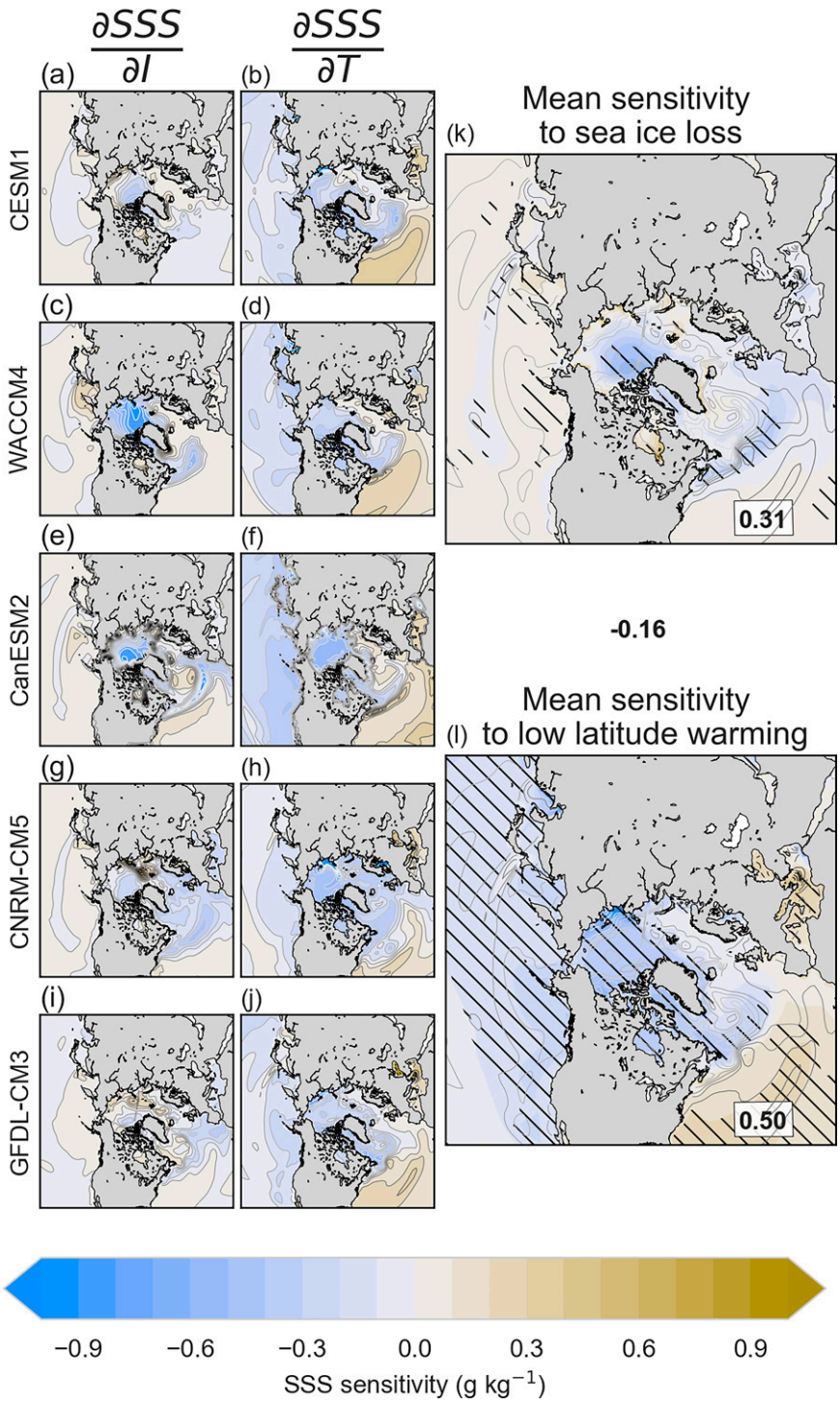

FIG. 11. As in Fig. 10, but for sea surface salinity.

what is seen in the surface temperature sensitivity (Fig. 4a), but opposite to that seen in the sensible and latent heat flux sensitivities (Figs. 9a,c), as previously noted. This robust pattern, found in all MEs to varying degrees, if driven by similar processes that drive variability in the PDO, results as a complex interplay of both local and remote atmospheric and oceanic processes (Newman et al. 2016). The decreased turbulent heat fluxes over the anomalously cool water shown in Figs. 9a and 9c act to damp SST changes by maintaining the SST gradient, increasing low-level baroclinicity and deepening

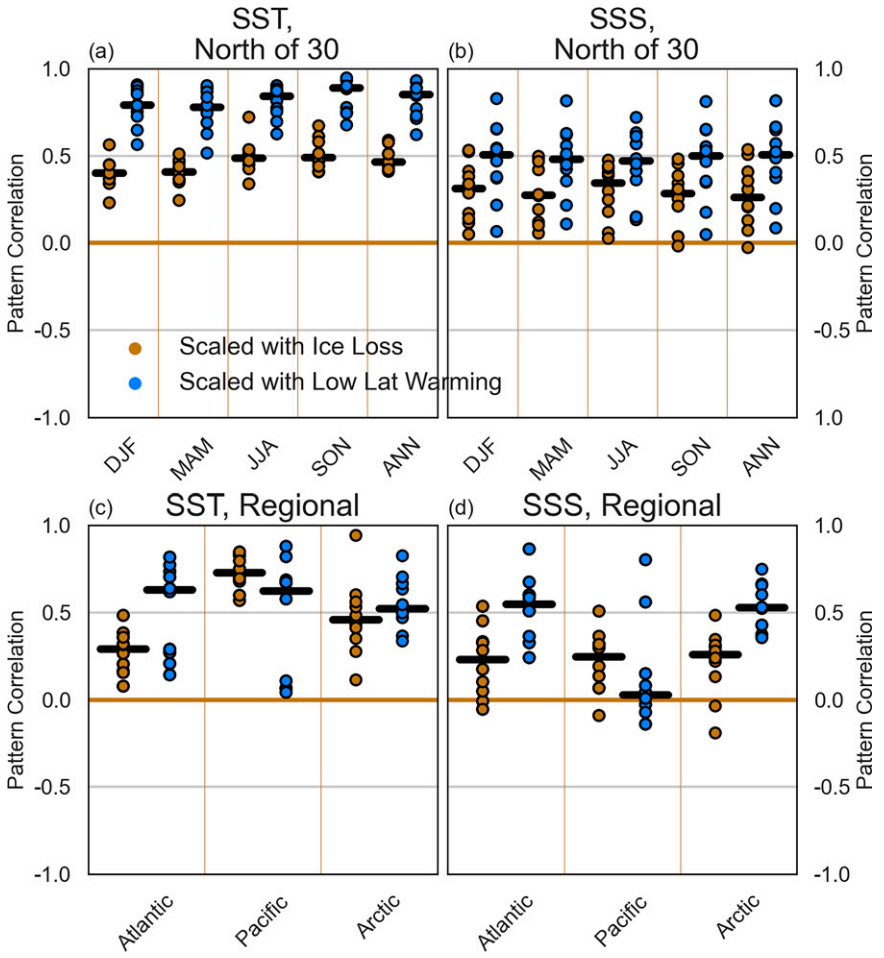

FIG. 12. As in Fig. 7, but for seasonal and annual mean (a) SST and (b) SSS. Also shown are inter-ME annual mean spatial correlations for the Atlantic, Pacific, and Arctic basins for (c) SST and (d) SSS. Blue symbols are correlations between SIL sensitivity patterns, and orange symbols are correlations between LLW sensitivity patterns.

the Aleutian low, which in turn reinforces the SST gradient by surface ocean divergence via a positive feedback (Zhang and Delworth 2015; Luo et al. 2020).

All MEs show at least some cooling in the North Atlantic that scales with SIL, although the location is not robust and is likely influenced by the mean states of the models, including biases and regions of deep ocean convection. One possible cause of subpolar cooling relative to the global mean is AMOC weakening (Drijfhout et al. 2012; Rahmstorf et al. 2015), and indeed all models considered here also simulate a weakening of the overturning circulation as a response to sea ice loss (not shown), in agreement with Sévellec et al. (2017), Liu and Fedorov (2019), and Liu et al. (2019). However, there are other physical processes that we cannot rule out, such as high-latitude ocean heat transport, that have also been identified as important for driving the warming hole (Keil et al. 2020).

The second column of Fig. 10 shows each ME's sensitivity to LLW, and the multi-ME mean is shown in Fig. 10l. As in the atmosphere, there is disagreement in the sign of the sensitivity in the Arctic, but otherwise there is a robust warming in most locations. The North Atlantic subpolar gyre region exhibits a "warming hole" in all models but CanESM2. The warming in the mean sensitivity is intensified in both the Gulf Stream and the Kuroshio relative to other regions, but we note considerable variability between MEs (e.g., CanESM2 does not exhibit intensified warming of the Kuroshio region, and CNRM-CM5 does not exhibit intensified warming of the Gulf Stream.)

We calculate inter-ME spatial correlations for the Northern Hemisphere oceans north of 30°N, as in section 3a (Fig. 12a), but we also subdivide that area into three ocean basins. Annual mean correlations calculated over the North Atlantic and the North Pacific, for 30°–60°N, and the Arctic Ocean, north of 60°N, are shown in Fig. 12c. There is little seasonal variation in the inter-ME correlations (Fig. 12a), especially in comparison with atmospheric surface temperatures (Fig. 7a) due to slower time scales of evolution in the ocean. The

exception to small interseasonal variability is a peak in correlations among the SIL sensitivity patterns in JJA and SON in the Atlantic relative to the other seasons (not shown). We reason that this is because the greatest forcing by sea ice loss on the ocean coincides with the seasons in which sea ice loss is greatest and is driven by the shortwave flux, unlike for the atmosphere whose response lags by at least a season and is driven by turbulent heat fluxes.

The median of inter-ME correlations for the Northern Hemisphere sensitivity to SIL is $r = 0.40$, while in the Pacific $r \approx 0.75$ year-round. In the Atlantic, the most robust season is JJA when the median $r = 0.7$; the colder seasons have lower correlations of $r = 0.25$. The median of inter-ME correlations in the sensitivity to LLW is greater in all seasons for the Northern Hemisphere. In the Atlantic and Pacific basins, the dots are clustered into two groups, where the lower correlations are the result of the CanESM2 sensitivity in the Pacific, and the GFDL CM3 sensitivity in the Atlantic, as noted above. In contrast to the atmospheric sensitivities, but in agreement with the surface flux variables, the pattern-scaled sensitivities to LLW are on average more robust than the SIL sensitivities. In the Arctic, we see a considerable spread in correlations, which might arise because the sensitivities are more closely tied to the details of ice loss here, which are in turn dependent on the ME (Fig. 2). This region is directly affected by the sea ice loss protocol, particularly in the MEs that introduce perturbations into the ocean either directly (e.g., CNRM-CM5) or indirectly through nudging the sea ice (WACCM4, CanESM2, and GFDL CM3).

The SSS sensitivities (Fig. 11) show that the sensitivity to LLW is more consistent across MEs (Fig. 11k) than the sensitivity to Arctic SIL (Fig. 11l). The agreement in the sensitivity to SIL is mainly confined to the Arctic, where there is a robust freshening of the central Arctic Ocean and salinification around the continental shelves, which may be indicating increased brine rejection as a consequence of more seasonal sea ice formation along the shelves. Outside the Arctic, we note a freshening in the extension of the Gulf Stream. On the other hand, the sensitivity to LLW indicates a clear and consistent freshening in the Pacific and Arctic Oceans that extends into the subpolar North Atlantic, and salinification of the rest of the Atlantic and the Mediterranean. This pattern reflects both observed and projected changes in salinity, which can be understood through the intensification of the hydrological cycle and manifests as an amplification of the mean pattern of salinity (Durack and Wijffels 2010; Skliris et al. 2014). Freshening of the Arctic Ocean in the sensitivity to LLW occurs in the absence of increased precipitation (see Fig. 4f), suggesting that it may be explained locally through reduced evaporation (see Fig. 9d), or remotely via ocean currents that carry relatively fresh Pacific Water through the Bering Strait, where they remain near the surface (Aagaard and Carmack 1989; Serreze et al. 2006), or even through increased precipitation over land, which scales with LLW (Fig. 4f) and increases river runoff into the Arctic Ocean (Nummelin et al. 2016). We do believe that we can rule out that this is an artifact of the sea ice loss protocol because all protocols are consistent in finding that the surface ocean under greenhouse warming will be fresher than under sea ice loss alone.

Correlations over the Northern Hemisphere as a whole (Fig. 12b) show minimal seasonality and reflect the relative robustness of the oceans LLW sensitivities in comparison with the SIL sensitivities. The median correlations in the Pacific are small for both sensitivities, so while the sign is consistent in the sensitivity to LLW, this reveals that the details of the pattern of freshening are not particularly robust. In the Arctic, despite a consistent sign in the sensitivity, as for SST, the low correlations among the pattern-scaled sensitivities to SIL reflects the differing patterns of sea ice loss and sea ice loss protocols. The lower inter-ME for the ocean sensitivities than for the atmosphere could also be due to the longer adjustment time scales of the ocean and the difference in length of the various model integrations (Table 1).

4. Discussion

Some aspects of the results warrant a more in-depth discussion. First, whether cooling of Eurasia is a forced response to Arctic sea ice loss in model experiments remains a topic of debate (Cohen et al. 2014; McCusker et al. 2016; Sun et al. 2016; Blackport et al. 2019; Mori et al. 2019a; Cohen et al. 2020; Labe et al. 2020), with these results suggesting it may play a minor role in the sensitivity to SIL in some models, as seen in Fig. 4a. However, this cooling is only weakly present in some of the coupled models' forced responses to Arctic sea ice loss (see Fig. 6a) and emerges more clearly only after we remove the back effect of LLW. In particular, Figs. 4c and 4d suggest that forced LLW acts to weaken the Siberian high in opposition to the forced response to SIL, which strengthens the Siberian high and cools by advection. Deser et al. (2016) found that coupling reduced Eurasian cooling relative to equivalent experiments run with an atmosphere-only model, a result also found comparing the atmosphere-only runs in England et al. (2018) with the coupled runs of England et al. (2020a,b). However, the Siberian high was found to be stronger in the coupled runs, and so the reduced cooling is not a dynamical response to LLW found in the coupled runs. Rather, it is likely related to the background mini global warming (which scales with LLW) or the stronger Arctic warming from the coupling advected over the continent. Beyond regional circulation changes, broader hemispheric warming coherent with LLW appears, in the models, to overwhelm any Eurasian cooling induced by SIL. Thus, if the models represent the global warming process accurately, such cooling is not likely to be observed as a long-term mean climate response under greenhouse warming. While these results on their own do not rule out the possibility that sea ice loss could enhance cold extremes, only that we should not expect cooling on average, other modeling studies have pointed to the reduced risk of cold extremes in response to sea ice loss because of reduced subseasonal variability (Screen et al. 2014, 2015; McCusker et al. 2016; Blackport and Kushner 2017; Collow et al. 2019). An additional note on this topic is that the model with the strongest cooling sensitivity in Eurasia is WACCM4 (not shown), suggesting the potential

importance of stratospheric dynamics in the development of that pattern of response, as has been previously found (Zhang et al. 2018). Last, recent work (He et al. 2020; Labe et al. 2020) has pointed out that the depth of Arctic amplification, which is not captured by our surface parameter–based pattern scaling approach, may be crucial to simulating Eurasian cooling. However, these studies do not suggest that the depth of Arctic warming is necessarily linked to sea ice loss, and we cannot rule out that the Arctic upper tropospheric warming arises from low-latitude warming.

Eurasian cooling from SIL is an example of the midlatitude "tug-of-war"-type responses where sea ice loss acts as a negative feedback on the response to lower-latitude warming (Harvey et al. 2014; Barnes and Polvani 2015; McCusker et al. 2017). Many of the mean pattern-scaled sensitivities were found to be negatively correlated with one another, such as the sea level pressure over Eurasia as just described, and similarly for the opposite-signed lower-tropospheric wind response in the west Pacific and in the zonal-mean zonal winds. For example, all MEs indicate a strengthening of the Siberian high in the sensitivity to SIL and a weakening of U850 winds in the Pacific (a weakening/equatorward shift of the Pacific storm track), a weakening of the Siberian high, and a poleward shift of the Pacific storm track in the sensitivity to LLW. Other negative feedbacks are found only in certain models, such as the finding that the sensitivity of the Aleutian low in CESM1 strengthens with SIL and weakens with LLW. While we do find overall that pattern-scaled sensitivities tend to be negatively correlated, we note that not all aspects of the sensitivities are robust in the multi-ME mean.

Last, the curious cooling of atmospheric surface temperature directly above the Arctic Ocean that scales with LLW is found in three of the five MEs considered here: CESM1, WACCM4, and CNRM-CM5. For the former two MEs, this counterintuitive result suggests that, per unit sea ice area loss, there is more warming in the dedicated sea ice loss experiment than in the transient RCP8.5 simulations. Because the sea ice distribution in WACCM4 is matched to that from the RCP8.5 simulation, it cannot be attributed to large differences in sea ice area (although small differences could be a factor); however, discrepancies in sea ice thickness may arise since it is not explicitly controlled for (England et al. 2020b). In the CMIP5 models, Feldl et al. (2020) found a negative lapse-rate feedback associated with remote changes rather than the positive lapse-rate feedback from local ones (e.g., sea ice loss), consistent with a negative lapse-rate feedback in the sensitivity to LLW using the same pattern-scaling method and CESM1 simulations we use here. The two models that have Arctic warming that scales with LLW use similar nudging protocols to lose sea ice and better match both thickness and area. It is therefore uncertain whether this Arctic cooling signal is a real physical response, an artifact of the ice loss protocol, or an artifact of the pattern-scaling decomposition. All of these possibilities warrant further investigation with, for example, an approach involving application of multiple ice-loss protocols, such as nudging and ghost forcing, in a single model to better elucidate mechanisms.

5. Conclusions

We have explored available simulations from five different coupled models designed to isolate the forced coupled climate response to sea ice loss as well as those that simulate the response to greenhouse warming. First, we have decomposed the forced responses into pattern-scaled sensitivities that scale with Arctic SIL and with LLW separately. Our results largely confirm the conclusions of Hay et al. (2018), which focused on just two of the model experiments used here. We find that the near-surface atmospheric sensitivity to SIL is surprisingly robust despite differences in sea ice loss protocols, background climate, and model physics. It consists of warming directly over the Arctic Ocean and over the high-latitude landmasses that extends up to 400 hPa, a dipole in sea level pressure with lower pressure over North America and high pressure over Eurasia, a weakening and equatorward shift of the storm tracks and jet that is more robust in the Pacific than in the Atlantic sector, and increased precipitation over the newly open Arctic and along the west coast of North America. The extratropical atmospheric sensitivity to SIL is generally more robust than the sensitivity to LLW in the cold season and near to the surface. However, in the warm season, the sensitivity to SIL is not robust among MEs, whereas the sensitivity to LLW is.

For the first time, we have applied pattern scaling to the forced surface ocean response (SST and SSS) and while there are greater inter-ME differences, we find a more robust sensitivity to LLW than to SIL in virtually all seasons and ocean basins, in general agreement with the sensitivities of surface heat fluxes. For both the surface ocean and the surface fluxes, the precise pattern of sea ice loss appears to be important in driving differences in the sensitivity to SIL, which is not the case for the atmospheric sensitivities. The sensitivity to LLW exhibits warming of the North Pacific and Atlantic intensified along the western boundary currents as well as freshening of the Pacific and Arctic Oceans (including the subpolar North Atlantic) and salinification of the Atlantic Ocean.

Taken together, the implications from the results presented here for the climate response to SIL provide a partially cohesive picture. The atmospheric sensitivity is generally quite robust, but it is difficult with the simulations at hand to determine whether some of the discrepancies that we are seeing are the result of differences in model physical parameterizations, of sensitivity to the mean state (Smith et al. 2017), of including a mix of transient and equilibrated simulations, or of including Arctic-only and global sea ice loss (with the latter being the case for the CESM1 low albedo simulation). While Sun et al. (2020) have shown that the sea ice loss protocol is unlikely to play a major role in the atmosphere or in the SST responses (although albedo forcing will likely result in a weaker response in DJF), whether the sea ice loss protocol is playing an important role in other aspects of the ocean response remains an open question. A downside to the pattern scaling approach we have taken is that it is not particularly helpful in understanding the underlying physics of the features it reveals and we are left to speculate. Fortunately, the Polar Amplification Model Intercomparison Project (Smith et al. 2019)

has the potential to include coordinated coupled modeling experiments with consistent sea ice loss protocols and target sea ice distributions, which should help elucidate some of the questions left open in this work.

Acknowledgments. This work is supported by a grant from the U.S. Department of Energy Grant DE-SC0019407. Author Polvani is supported, in part, by a grant from the U.S. National Science Foundation to Columbia University. The National Center for Atmospheric Research is sponsored by the National Science Foundation.

REFERENCES

Aagaard, K., and E. C. Carmack, 1989: The role of sea ice and other fresh water in the Arctic circulation. *J. Geophys. Res.*, **94**, 14485, https://doi.org/10.1029/JC094iC10p14485.

Barnes, E. A., and L. M. Polvani, 2015: CMIP5 projections of Arctic amplification, of the North American/North Atlantic circulation, and of their relationship. *J. Climate*, **28**, 5254–5271, https://doi.org/10.1175/JCLI-D-14-00589.1.

——, and J. A. Screen, 2015: The impact of Arctic warming on the midlatitude jet-stream: Can it? Has it? Will it? *Wiley Interdiscip. Rev.: Climate Change*, **6**, 277–286, https://doi.org/10.1002/wcc.337.

Bichet, A., P. J. Kushner, L. Mudryk, L. Terray, and J. C. Fyfe, 2015: Estimating the anthropogenic sea surface temperature response using pattern scaling. *J. Climate*, **28**, 3751–3763, https://doi.org/10.1175/JCLI-D-14-00604.1.

Bintanja, R., and F. M. Selten, 2014: Future increases in Arctic precipitation linked to local evaporation and sea-ice retreat. *Nature*, **509**, 479–482, https://doi.org/10.1038/nature13259.

Blackport, R., and P. J. Kushner, 2016: The transient and equilibrium climate response to rapid summertime sea ice loss in CCSM4. *J. Climate*, **29**, 401–417, https://doi.org/10.1175/JCLI-D-15-0284.1.

——, and ——, 2017: Isolating the atmospheric circulation response to Arctic sea ice loss in the coupled climate system. *J. Climate*, **30**, 2163–2185, https://doi.org/10.1175/JCLI-D-16-0257.1.

——, and J. A. Screen, 2020: Insignificant effect of Arctic amplification on the amplitude of midlatitude atmospheric waves. *Sci. Adv.*, **6**, eaay2880, https://doi.org/10.1126/sciadv.aay2880.

——, ——, K. van der Wiel, and R. Bintanja, 2019: Minimal influence of reduced Arctic sea ice on coincident cold winters in mid-latitudes. *Nat. Climate Change*, **9**, 697–704, https://doi.org/10.1038/s41558-019-0551-4.

Cohen, J., and Coauthors, 2014: Recent Arctic amplification and extreme mid-latitude weather. *Nat. Geosci.*, **7**, 627–637, https://doi.org/10.1038/ngeo2234.

——, and Coauthors, 2020: Divergent consensuses on Arctic amplification influence on midlatitude severe winter weather. *Nat. Res.*, 20–29, https://doi.org/10.1038/s41558-019-0662-y.

Collow, T. W., W. Wang, and A. Kumar, 2019: Reduction in northern midlatitude 2-m temperature variability due to Arctic sea ice loss. *J. Climate*, **32**, 5021–5035, https://doi.org/10.1175/JCLI-D-18-0692.1.

Deng, J., A. Dai, and H. Xu, 2020: Nonlinear climate responses to increasing CO_2 and anthropogenic aerosols simulated by CESM1. *J. Climate*, **33**, 281–301, https://doi.org/10.1175/JCLI-D-19-0195.1.

Deser, C., R. Tomas, M. Alexander, and D. Lawrence, 2010: The seasonal atmospheric response to projected Arctic sea ice loss in the late twenty-first century. *J. Climate*, **23**, 333–351, https://doi.org/10.1175/2009JCLI3053.1.

——, R. A. Tomas, and L. Sun, 2015: The role of ocean–atmosphere coupling in the zonal-mean atmospheric response to Arctic sea ice loss. *J. Climate*, **28**, 2168–2186, https://doi.org/10.1175/JCLI-D-14-00325.1.

——, L. Sun, R. A. Tomas, and J. Screen, 2016: Does ocean coupling matter for the northern extratropical response to projected Arctic sea ice loss? *Geophys. Res. Lett.*, **43**, 2149–2157, https://doi.org/10.1002/2016GL067792.

Drijfhout, S., G. J. van Oldenborgh, and A. Cimatoribus, 2012: Is a decline of AMOC causing the warming hole above the North Atlantic in observed and modeled warming patterns? *J. Climate*, **25**, 8373–8379, https://doi.org/10.1175/JCLI-D-12-00490.1.

Durack, P. J., and S. E. Wijffels, 2010: Fifty-year trends in global ocean salinities and their relationship to broad-scale warming. *J. Climate*, **23**, 4342–4362, https://doi.org/10.1175/2010JCLI3377.1.

England, M., L. M. Polvani, and L. Sun, 2018: Contrasting the Antarctic and Arctic atmospheric responses to projected sea ice loss in the late twenty-first century. *J. Climate*, **31**, 6353–6370, https://doi.org/10.1175/JCLI-D-17-0666.1.

——, ——, and ——, 2020a: Robust Arctic warming caused by projected Antarctic sea ice loss. *Environ. Res. Lett*, **15**, 104005, https://doi.org/10.1088/1748-9326/abaada.

——, ——, ——, and C. Deser, 2020b: Tropical climate responses to projected Arctic and Antarctic sea-ice loss. *Nat. Geosci.*, **13**, 275–281, https://doi.org/10.1038/s41561-020-0546-9.

Feldl, N., S. Po-Chedley, H. K. A. Singh, S. Hay, and P. J. Kushner, 2020: Sea ice and atmospheric circulation shape the high-latitude lapse rate feedback. *npj Climate Atmos. Sci.*, **3**, 41, https://doi.org/10.1038/s41612-020-00146-7.

Harvey, B. J., L. C. Shaffrey, and T. J. Woollings, 2014: Equator-to-pole temperature differences and the extra-tropical storm track responses of the CMIP5 climate models. *Climate Dyn.*, **43**, 1171–1182, https://doi.org/10.1007/s00382-013-1883-9.

Hay, S., P. J. Kushner, R. Blackport, and K. E. McCusker, 2018: On the relative robustness of the climate response to high-latitude and low-latitude warming. *Geophys. Res. Lett.*, **45**, 6232–6241, https://doi.org/10.1029/2018GL077294.

He, S., X. Xu, T. Furevik, and Y. Gao, 2020: Eurasian cooling linked to the vertical distribution of Arctic warming. *Geophys. Res. Lett.*, **47**, e2020GL087212, https://doi.org/10.1029/2020GL087212.

Herger, N., B. M. Sanderson, and R. Knutti, 2015: Improved pattern scaling approaches for the use in climate impact studies. *Geophys. Res. Lett.*, **42**, 3486–3494, https://doi.org/10.1002/2015GL063569.

Kay, J. E., and Coauthors, 2015: The Community Earth System Model (CESM) Large Ensemble Project: A community resource for studying climate change in the presence of internal climate variability. *Bull. Amer. Meteor. Soc.*, **96**, 1333–1349, https://doi.org/10.1175/BAMS-D-13-00255.1.

Keil, P., T. Mauritsen, J. Jungclaus, C. Hedemann, D. Olonscheck, and R. Ghosh, 2020: Multiple drivers of the North Atlantic warming hole. *Nat. Climate Change*, **10**, 667–671, https://doi.org/10.1038/s41558-020-0819-8.

Labe, Z., Y. Peings, and G. Magnusdottir, 2020: Warm Arctic, cold Siberia pattern: Role of full Arctic amplification versus sea ice loss alone. *Geophys. Res. Lett.*, **47**, e2020GL088583, https://doi.org/10.1029/2020GL088583.

Lee, S., C. Woods, and R. Caballero, 2019: Relation between Arctic moisture flux and tropical temperature biases in CMIP5 simulations and its fingerprint in RCP8.5 projections. *Geophys. Res. Lett.*, **46**, 1088–1096, https://doi.org/10.1029/2018GL080562.

Liang, Y., and Coauthors, 2020: Quantification of the Arctic sea ice-driven atmospheric circulation variability in coordinated large ensemble simulations. *Geophys. Res. Lett.*, **47**, e2019GL085397, https://doi.org/10.1029/2019GL085397.

Liu, W., and A. V. Fedorov, 2019: Global impacts of Arctic sea ice loss mediated by the Atlantic meridional overturning circulation. *Geophys. Res. Lett.*, **46**, 944–952, https://doi.org/10.1029/2018GL080602.

——, ——, and F. Sévellec, 2019: The mechanisms of the Atlantic meridional overturning circulation slowdown induced by Arctic sea ice decline. *J. Climate*, **32**, 977–996, https://doi.org/10.1175/JCLI-D-18-0231.1.

Luo, H., F. Zheng, N. Keenlyside, and J. Zhu, 2020: Ocean–atmosphere coupled Pacific decadal variability simulated by a climate model. *Climate Dyn.*, **54**, 4759–4773, https://doi.org/10.1007/s00382-020-05248-9.

Lynch, C., C. Hartin, B. Bond-Lamberty, and B. Kravitz, 2016: Exploring global surface temperature pattern scaling methodologies and assumptions from a CMIP5 model ensemble. *Geosci. Model Dev. Discuss.*, https://doi.org/10.5194/gmd-2016-170.

Marsh, D. R., and Coauthors, 2013: Climate change from 1850 to 2005 simulated in CESM1(WACCM). *J. Climate*, **26**, 7372–7391, https://doi.org/10.1175/JCLI-D-12-00558.1.

Marvel, K., G. A. Schmidt, D. Shindell, C. Bonfils, A. N. Legrande, L. Nazarenko, and K. Tsigaridis, 2015: Do responses to different anthropogenic forcings add linearly in climate models? *Environ. Res. Lett.*, **10**, 104010, https://doi.org/10.1088/1748-9326/10/10/104010.

McCusker, K. E., J. C. Fyfe, and M. Sigmond, 2016: Twenty-five winters of unexpected Eurasian cooling unlikely due to Arctic sea-ice loss. *Nat. Geosci.*, **9**, 838–842, https://doi.org/10.1038/ngeo2820.

——, P. J. Kushner, J. C. Fyfe, M. Sigmond, V. V. Kharin, and C. M. Bitz, 2017: Remarkable separability of circulation response to Arctic sea ice loss and greenhouse gas forcing. *Geophys. Res. Lett.*, **44**, 7955–7964, https://doi.org/10.1002/2017GL074327.

Mitchell, T. D., 2003: Pattern scaling: An examination of the accuracy of the technique for describing future climates. *Climatic Change*, **60**, 217–242, https://doi.org/10.1023/A:1026035305597.

Mori, M., M. Watanabe, H. Shiogama, J. Inoue, and M. Kimoto, 2014: Robust Arctic sea-ice influence on the frequent Eurasian cold winters in past decades. *Nat. Geosci.*, **7**, 869–873, https://doi.org/10.1038/ngeo2277.

——, Y. Kosaka, M. Watanabe, H. Nakamura, and M. Kimoto, 2019a: A reconciled estimate of the influence of Arctic sea-ice loss on recent Eurasian cooling. *Nat. Climate Change*, **9**, 123–129, https://doi.org/10.1038/s41558-018-0379-3.

——, ——, ——, B. Taguchi, H. Nakamura, and M. Kimoto, 2019b: Reply to: Is sea-ice-driven Eurasian cooling too weak in models? *Nat. Climate Change*, **9**, 937–939, https://doi.org/10.1038/s41558-019-0636-0.

Newman, M., and Coauthors, 2016: The Pacific decadal oscillation, revisited. *J. Climate*, **29**, 4399–4427, https://doi.org/10.1175/JCLI-D-15-0508.1.

Nummelin, A., M. Ilicak, C. Li, and L. H. Smedsrud, 2016: Consequences of future increased Arctic runoff on Arctic Ocean stratification, circulation, and sea ice cover. *J. Geophys. Res. Oceans*, **121**, 617–637, https://doi.org/10.1002/2015JC011156.

Ogawa, F., and Coauthors, 2018: Evaluating impacts of recent Arctic sea ice loss on the Northern Hemisphere winter climate change. *Geophys. Res. Lett.*, **45**, 3255–3263, https://doi.org/10.1002/2017GL076502.

Oudar, T., E. Sanchez-Gomez, F. Chauvin, J. Cattiaux, L. Terray, and C. Cassou, 2017: Respective roles of direct GHG radiative forcing and induced Arctic sea ice loss on the Northern Hemisphere atmospheric circulation. *Climate Dyn.*, **49**, 3693–3713, https://doi.org/10.1007/s00382-017-3541-0.

Overland, J., J. A. Francis, R. Hall, E. Hanna, S.-J. Kim, and T. Vihma, 2015: The melting Arctic and midlatitude weather patterns: Are they connected? *J. Climate*, **28**, 7917–7932, https://doi.org/10.1175/JCLI-D-14-00822.1.

Peings, Y., and G. Magnusdottir, 2014: Response of the wintertime Northern Hemisphere atmospheric circulation to current and projected Arctic sea ice decline: A numerical study with CAM5. *J. Climate*, **27**, 244–264, https://doi.org/10.1175/JCLI-D-13-00272.1.

——, J. Cattiaux, and G. Magnusdottir, 2019: The polar stratosphere as an arbiter of the projected tropical versus polar tug of war. *Geophys. Res. Lett.*, **46**, 9261–9270, https://doi.org/10.1029/2019GL082463.

Petrie, R. E., L. C. Shaffrey, and R. T. Sutton, 2015: Atmospheric response in summer linked to recent Arctic sea ice loss. *Quart. J. Roy. Meteor. Soc.*, **141**, 2070–2076, https://doi.org/10.1002/qj.2502.

Rahmstorf, S., J. E. Box, G. Feulner, M. E. Mann, A. Robinson, S. Rutherford, and E. J. Schaffernicht, 2015: Exceptional twentieth-century slowdown in Atlantic Ocean overturning circulation. *Nat. Climate Change*, **5**, 475–480, https://doi.org/10.1038/nclimate2554.

Santer, B. D., T. M. L. Wigley, M. E. Schelsinger, and J. F. B. Mitchell, 1990: Developing climate scenarios from equilibrium GCM results. Max-Planck-Institut für Meteorologie Tech. Rep. 47, 29 pp., https://mpimet.mpg.de/fileadmin/publikationen/Reports/Report_47.pdf.

Screen, J. A., and R. Blackport, 2019a: How robust is the atmospheric response to projected Arctic sea ice loss across climate models? *Geophys. Res. Lett.*, **46**, 11 406–11 415, https://doi.org/10.1029/2019GL084936.

——, and ——, 2019b: Is sea-ice-driven Eurasian cooling too weak in models? *Nat. Climate Change*, **9**, 934–936, https://doi.org/10.1038/s41558-019-0635-1.

——, C. Deser, and I. Simmonds, 2012: Local and remote controls on observed Arctic warming. *Geophys. Res. Lett.*, **39**, L10709, https://doi.org/10.1029/2012GL051598.

——, ——, ——, and R. Tomas, 2014: Atmospheric impacts of Arctic sea-ice loss, 1979–2009: Separating forced change from atmospheric internal variability. *Climate Dyn.*, **43**, 333–344, https://doi.org/10.1007/s00382-013-1830-9.

——, ——, and L. Sun, 2015: Projected changes in regional climate extremes arising from Arctic sea ice loss. *Environ. Res. Lett.*, **10**, 084006, https://doi.org/10.1088/1748-9326/10/8/084006.

——, and Coauthors, 2018: Consistency and discrepancy in the atmospheric response to Arctic sea-ice loss across climate models. *Nat. Geosci.*, **11**, 155–163, https://doi.org/10.1038/s41561-018-0059-y.

Serreze, M. C., and Coauthors, 2006: The large-scale freshwater cycle of the Arctic. *J. Geophys. Res.*, **111**, C11010, https://doi.org/10.1029/2005JC003424.

Sévellec, F., A. V. Fedorov, and W. Liu, 2017: Arctic sea-ice decline weakens the Atlantic meridional overturning circulation. *Nat. Climate Change*, **7**, 604–610, https://doi.org/10.1038/nclimate3353.

Shiogama, H., D. A. Stone, T. Nagashima, T. Nozawa, and S. Emori, 2013: On the linear additivity of climate forcing-response relationships at global and continental scales. *Int. J. Climatol.*, **33**, 2542–2550, https://doi.org/10.1002/joc.3607.

Skliris, N., R. Marsh, S. A. Josey, S. A. Good, C. Liu, and R. P. Allan, 2014: Salinity changes in the World Ocean since 1950 in relation to changing surface freshwater fluxes. *Climate Dyn.*, **43**, 709–736, https://doi.org/10.1007/s00382-014-2131-7.

Smith, D. M., N. J. Dunstone, A. A. Scaife, E. K. Fiedler, D. Copsey, and S. C. Hardiman, 2017: Atmospheric response to Arctic and Antarctic sea ice: The importance of ocean–atmosphere coupling and the background state. *J. Climate*, **30**, 4547–4546, https://doi.org/10.1175/JCLI-D-16-0564.1.

——, and Coauthors, 2019: The Polar Amplification Model Intercomparison Project (PAMIP) contribution to CMIP6: Investigating the causes and consequences of polar amplification. *Geosci. Model Dev.*, **12**, 1139–1164, https://doi.org/10.5194/gmd-12-1139-2019.

Stott, P. A., N. P. Gillett, G. C. Hegerl, D. J. Karoly, D. A. Stone, X. Zhang, and F. Zwiers, 2010: Detection and attribution of climate change: A regional perspective. *Wiley Interdiscip. Rev.: Climate Change*, **1**, 192–211, https://doi.org/10.1002/wcc.34.

Sun, L., C. Deser, and R. A. Tomas, 2015: Mechanisms of stratospheric and tropospheric circulation response to projected Arctic sea ice loss. *J. Climate*, **28**, 7824–7845, https://doi.org/10.1175/JCLI-D-15-0169.1.

——, J. Perlwitz, and M. Hoerling, 2016: What caused the recent "warm Arctic, cold continents" trend pattern in winter temperatures? *Geophys. Res. Lett.*, **43**, 5345–5352, https://doi.org/10.1002/2016GL069024.

——, M. Alexander, and C. Deser, 2018: Evolution of the global coupled climate response to Arctic sea ice loss during 1990–2090 and its contribution to climate change. *J. Climate*, **31**, 7823–7843, https://doi.org/10.1175/JCLI-D-18-0134.1.

——, C. Deser, R. A. Tomas, and M. Alexander, 2020: Global coupled climate response to polar sea ice loss: Evaluating the effectiveness of different ice-constraining approaches. *Geophys. Res. Lett.*, **47**, e2019GL085788, https://doi.org/10.1029/2019GL085788.

Tebaldi, C., and J. M. Arblaster, 2014: Pattern scaling: Its strengths and limitations, and an update on the latest model simulations. *Climatic Change*, **122**, 459–471, https://doi.org/10.1007/s10584-013-1032-9.

Tomas, R. A., C. Deser, L. Sun, R. A. T. And, and C. Deser, 2016: The role of ocean heat transport in the global climate response to projected Arctic sea ice loss. *J. Climate*, **29**, 6841–6859, https://doi.org/10.1175/JCLI-D-15-0651.1.

Vihma, T., 2014: Effects of Arctic sea ice decline on weather and climate: A review. *Surv. Geophys.*, **35**, 1175–1214, https://doi.org/10.1007/s10712-014-9284-0.

Wang, K., C. Deser, L. Sun, and R. A. Tomas, 2018: Fast response of the tropics to an abrupt loss of Arctic sea ice via ocean dynamics. *Geophys. Res. Lett.*, **45**, 4264–4272, https://doi.org/10.1029/2018GL077325.

Zappa, G., P. Ceppi, and T. G. Shepherd, 2021: Eurasian cooling in response to Arctic sea-ice loss is not proved by maximum covariance analysis. *Nat. Climate Change*, **11**, 106–108, https://doi.org/10.1038/s41558-020-00982-8.

Zhang, L., and T. L. Delworth, 2015: Analysis of the characteristics and mechanisms of the Pacific decadal oscillation in a suite of coupled models from the Geophysical Fluid Dynamics Laboratory. *J. Climate*, **28**, 7678–7701, https://doi.org/10.1175/JCLI-D-14-00647.1.

Zhang, P., Y. Wu, I. R. Simpson, K. L. Smith, X. Zhang, B. De, and P. Callaghan, 2018: A stratospheric pathway linking a colder Siberia to Barents-Kara Sea ice loss. *Sci. Adv.*, **4**, eaat6025, https://doi.org/10.1126/sciadv.aat6025.